



HAL
open science

Insights from synthetic seismogram modelling study of oceanic lower crust and Moho Transition Zone

Vaibhav Ingale, Satish C. Singh

► **To cite this version:**

Vaibhav Ingale, Satish C. Singh. Insights from synthetic seismogram modelling study of oceanic lower crust and Moho Transition Zone. *Tectonophysics*, 2021, 816, 11 pp. 10.1016/j.tecto.2021.229030 . insu-03589885

HAL Id: insu-03589885

<https://insu.hal.science/insu-03589885>

Submitted on 16 Oct 2023

HAL is a multi-disciplinary open access archive for the deposit and dissemination of scientific research documents, whether they are published or not. The documents may come from teaching and research institutions in France or abroad, or from public or private research centers.

L'archive ouverte pluridisciplinaire **HAL**, est destinée au dépôt et à la diffusion de documents scientifiques de niveau recherche, publiés ou non, émanant des établissements d'enseignement et de recherche français ou étrangers, des laboratoires publics ou privés.



Distributed under a Creative Commons Attribution - NonCommercial 4.0 International License

1 **Insights from synthetic seismogram modelling study of oceanic lower crust and Moho** 2 **Transition Zone**

3 Vaibhav Ingale and Satish C. Singh*

4
5 Université de Paris, Institut de Physique du Globe de Paris, CNRS, Paris, France

6
7 Corresponding author: Satish Singh (singh@ipgp.fr)

8 9 **Abstract**

10 The Moho discontinuity is one of the fundamental boundaries on Earth, separating the crust
11 from the upper mantle. Arrival times of seismic reflection and refraction data are used to estimate
12 the depth of the Moho, but the nature of the Moho remains illusive. We present a synthetic
13 seismogram modelling study for a suite of possible velocity models of the oceanic lower crust and
14 Moho transition zone (MTZ). For modelling, we have used a 45-km long multichannel streamer
15 (MCS) geometry, to get insight about waveforms and amplitudes of seismic phases like the crustal
16 refraction (Pg), Moho reflection (PmP) and mantle refraction (Pn), and the interactions between
17 these phases. We find that the nature of PmP reflection not only depends on the velocity structure of
18 the MTZ but also on the velocity structure of the lower crust and upper mantle. The triplication
19 resulting from these three seismic arrivals and its lateral extent mainly depend on the velocity
20 structure in the lower crust. Apart from the velocity in the crust, the critical distance for the PmP
21 arrival depends on the velocity gradient in the MTZ. The amplitude versus offset analysis of the
22 wide-angle PmP arrivals indicates that there are two broad high amplitude peaks for the MTZ
23 thickness less than or equal to the dominant seismic wavelength and only one large narrow peak for
24 a thicker MTZ. Consequently, strong PmP arrivals for a thick MTZ lie in a narrow offset range
25 around the critical offset whereas they lie over a large offset range for a sharp Moho. We also have
26 modelled the synthetic seismograms for velocity structures from the Oman and the Bay of Islands
27 ophiolites. Our modelling results indicate that the quantitative analysis of amplitudes and
28 waveforms of ultra-long offset MCS data could provide detailed information about the lower crust
29 and MTZ.

30
31 **Keywords:** Synthetic Seismogram; Lower Crust; Moho Transition Zone; Reflection and Refraction
32 arrivals; Amplitude Variation with Offset; Triplication

35

36 **1 Introduction**

37

38 Based on the observation of wide-angle reflection arrivals from an earthquake on October 8,
39 1909, Andrija Mohorovičić [1910] suggested that there should be a boundary between the lower
40 continental crust and the upper mantle, which was later termed as the Moho. Soon after the Second
41 World War, active source seismic experiments led by Ewing and Press [1950, 1952] in the Atlantic
42 Ocean and Raitt [1956] in the Pacific Ocean allowed the discovery of the oceanic Moho. They
43 found that the crustal P-wave velocity in the oceanic domain is higher than those observed on
44 continents, suggesting that the oceanic crust is possibly composed of basaltic/gabbroic rocks above
45 mantle rocks, separated by the Moho, where the Moho is a lithological boundary. Hess [1962], on
46 the other hand, suggested that the oceanic Moho might be a serpentinization front, separating
47 serpentinized peridotite in the lower crust with pure peridotite in the mantle. Since then many
48 seismic experiments (reflection and refraction) have been carried out to determine the crustal
49 thickness and velocity structures in different ocean basins from different spreading environments,
50 which are well documented by White et al. [1992], Mutter and Carton [2013] and Christeson et al.
51 [2019].

52

53 Seismic reflection experiments in the Pacific Ocean, where the oceanic crust is formed in
54 fast and intermediate spreading environments, showed reflections 2-3 s below the basement away
55 from the ridge axis, suggesting that there should be a sharp P-wave velocity contrast at the Moho
56 [Herron et al. 1980; Kent et al. 1994; Barth, 1994; Barth and Mutter, 1996; Mutter and Carton,
57 2013; Aghaei et al. 2014]. Using a 3D seismic imaging technique, Singh et al. [2006] imaged a
58 reflection from the Moho beneath the ridge axis, and suggested that the Moho is formed at zero age.
59 Based on the reflection characters, Kent et al. [1994] identified three types of Moho reflections,
60 which they termed as impulsive, shingled or diffused. When the Moho transition zone (transition
61 zone between oceanic lower crust and upper mantle; MTZ) is thin, then single phase impulsive
62 (continuous) and shingled (discontinuous; broken in smaller sections) reflections are observed
63 [Brocher et al. 1985; Nedimović et al. 2005]. However, when the MTZ becomes thick (e.g. gradient
64 zone), then the Moho reflection becomes multiphase and diffusive, even may disappear [Collins et
65 al. 1986; Ohira et al. 2017]. Although continuous Moho reflections have been observed in fast and
66 intermediate spreading environments, they have been only intermittently imaged in slow spreading
67 oceanic environments (e.g. [Morris et al. 1993; McBride et al. 1994; Mehouchi and Singh, 2018]),
68 and never observed in ultra-slow spreading environments. Even though near or zero offset seismic
69 reflection data can provide a seismic image of the Moho [Eittrheim et al. 1994; Barth and Mutter,
70 1996], they do not provide any quantitative information about the nature of the Moho [Mutter and

71 Carton, 2013]. Since the streamers used in seismic reflection experiments are generally short (3-6
72 km long), these data do not provide much information about the velocity in the crust, and hence
73 most of the seismic images are interpreted in two-way vertical travel time. In order to convert these
74 images into depth, crustal velocity information is required, which is commonly obtained using
75 wide-angle seismic (refraction and reflection) data.

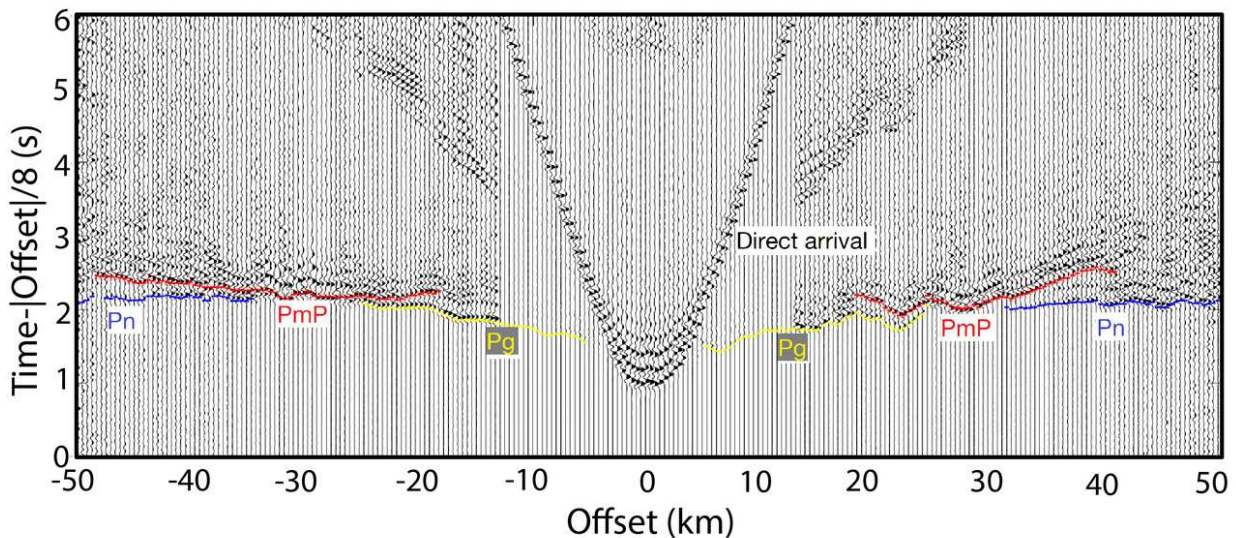
76

77 Initially wide-angle data were acquired either using disposable sonobuoy [e.g. Raitt, 1956]
78 or two ship expanding spread profiles [Stoffa and Buhl, 1979; Harding et al. 1989; Vera et al.
79 1990], and simple 1D slope-intercept time methods were used to determine crustal velocities and
80 Moho depths [e.g. Stoffa et al. 1981]. These data recorded crustal refraction (Pg) arrivals, mantle
81 refraction (Pn) arrivals and wide-angle reflection from the Moho (PmP) (see Figure 1) [Vaddineni
82 et al. 2021]. The advent of ocean bottom seismometers (OBS) and tomographic methods have
83 allowed to better quantify the oceanic crustal velocities and crustal thicknesses [Christeson et al.
84 2019]. White et al. [1992] synthesised crustal thickness using these data and found that the crustal
85 thickness varies from 5.8 to 8.5 km with an average of 7.1 ± 0.8 km. Christeson et al. [2019] have
86 recently updated this analysis and find an average crustal thickness of 6.15 km, which is
87 independent of spreading rates. All these wide-angle results suggest that the oceanic crust consists
88 principally of two layers; an upper crust (Layer 2) with a high velocity gradient and a lower crust
89 (Layer 3) with a low velocity gradient. As the velocity gradient in the lower crust is generally low,
90 and Pg and PmP arrivals overlap beyond critical distance, the arrival times of crustal arrivals (Pg)
91 only constrain the velocity information of the upper crust [Vaddineni et al. 2021], whereas the
92 velocity in the lower crust and the Moho depth are constrained by PmP arrival time. Although the
93 PmP rays travel through the lower crust, there is a trade-off between lower crustal velocities and
94 Moho depth [Mjelde, 1992; Cook et al. 2010, Vaddineni et al. 2021]. Furthermore, in most of the
95 wide-angle tomographic analyses, the Moho is defined as a reflection interface, and hence these
96 methods do not provide any information about the nature of Moho or MTZ.

97

98 The petrological study of ophiolites has allowed to link seismological results with lithology
99 and shed light on the formation and evolution of the oceanic crust and Moho. According to the
100 Penrose model [Penrose, 1972], the upper crust (Layer 2) consists of pillow lavas (Layer 2A) and
101 dikes (Layer 2B) and the lower crust (Layer 3) of homogeneous gabbro. Insights obtained from the
102 Oman ophiolite [Quick and Denlinger, 1993], the presence of upper crustal melt lens [Detrick et al.
103 1987; Kent et al. 1990] and the low velocity anomaly in the lower crustal [Harding et al. 1989; Vera
104 et al. 1990; Toomey et al. 1990] beneath fast and intermediate spreading ridges led to the suggestion
105 that the lower crust is formed by cooling and crystallisation of melt in the upper crustal melt lens
106 and subsequent subsidence, which is termed as the gabbro glacier model [Henstock et al. 1993]. But

107 some other studies of the Oman Ophiolite [Boudier et al. 1996; Kelemen et al. 1997] indicated the
108 presence of secondary melt sills in the lower crust, suggesting that the lower crust could be formed
109 by melt sill injection in the lower crust, termed as the sheeted sill model.
110

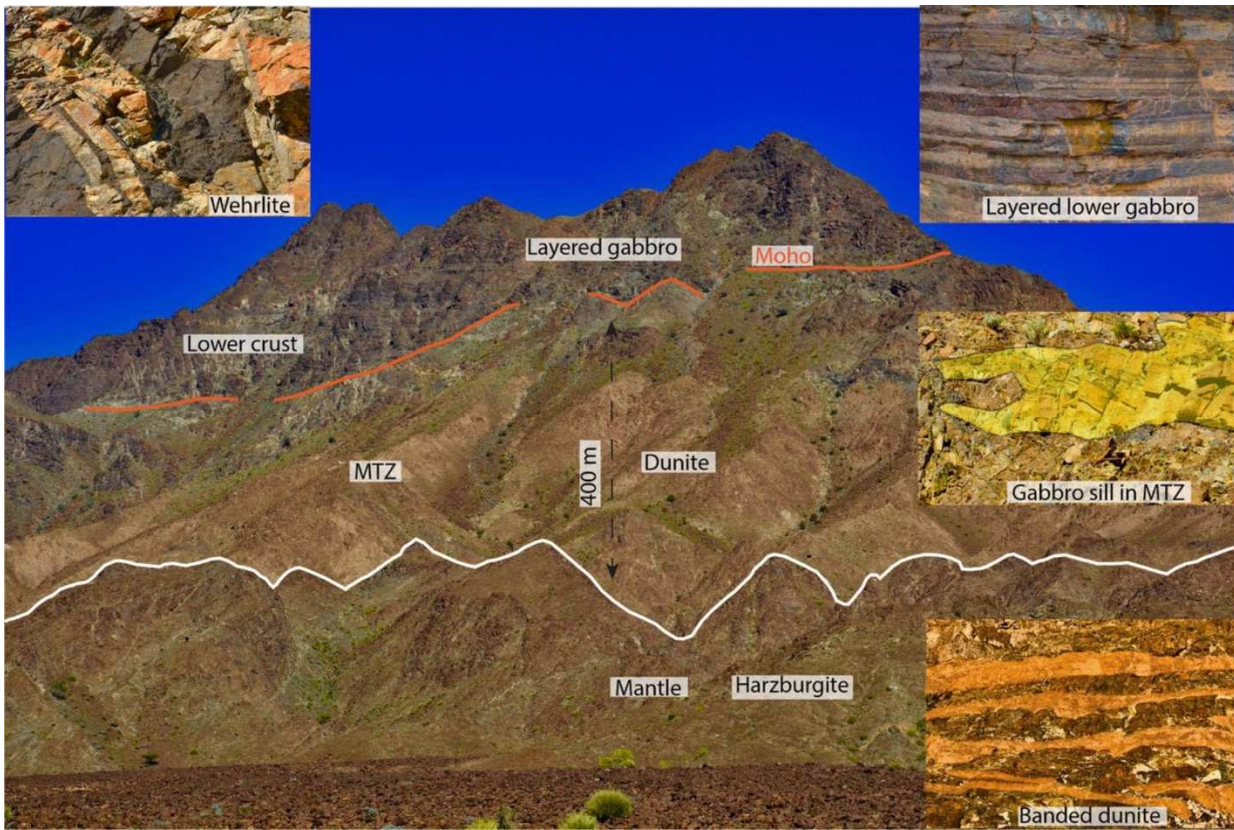


111
112 **Figure 1: Wide-angle seismic data:** Wide-angle seismic data recorded on one of the OBS55 of LITHOS
113 profile [Vaddineni et al. 2021], showing the crustal (Pg), mantle (Pn) arrivals and PmP reflection from
114 Moho. The vertical axis is the reduced travel time with a reduction velocity of 8 km/s and the horizontal axis
115 is the source-receiver offset.

116
117 There are two types of layering observed in the Oman Ophiolite, layered gabbro and
118 gradational layering. The layered gabbro consists of 10 cm to 100 m thick layers of different types
119 of homogeneous gabbros with sharp boundaries [Boudier et al. 1996]. In the gradational layering,
120 the crystal sizes are large at the bottom of the section and gradually become finer towards the upper
121 section of the gabbro [Boudier et al. 1996]. In the last decade, multiple melt sill reflections have
122 been imaged beneath the East Pacific Rise [Arnulf et al. 2015; Marjanovic et al. 2015] and the Juan
123 du Fuca Ridge [Carbotte et al. 2020]. Very recently, Guo et al. [2021a] have imaged seismic
124 layering in the lower crust for a crust formed at the slow spreading Mid-Atlantic Ridge between 7
125 and 13 Myr, indicating that the lower oceanic crust might indeed be formed in situ by melt sill
126 injection and cooling and crystallisation in the lower crust.

127
128 Studies of ophiolites have also provided insight about the MTZ. For example, the MTZ
129 could be sharp and/or up to 750 m thick in the Oman ophiolite (Figure 2) [Boudier and Nicolas,
130 1995; Joussetin and Nicolas, 2000; Joussetin et al. 2012] and a couple of kilometres thick in the Bay
131 of Islands ophiolite [Kempner and Gettrust, 1982; Karson et al. 1984]. One of the authors (Singh)
132 travelled to Oman three times, twice with Professor Adolphe Nicolas who inspired this study, and

133 he recently visited Oman in January 2020 (see Figure 2). The crust in the Oman ophiolite is
134 supposed to have formed at a fast spreading ridge, and has been used as a typical example of a fast
135 spreading crust [Nicolas et al. 1996]. The presence of layered gabbros and a sharp Moho is
136 consistent with this hypothesis. On the other hand, the crust in the Bay of Islands ophiolite was
137 supposed to have formed in a slow spreading environment [Kempner and Gettrust, 1982]. The
138 geology in the Bay of Islands is more complex, where both the crust and the MTZ are more
139 heterogeneous. Although the lower crustal gabbros are well preserved in ophiolites, peridotites and
140 dunites are heavily serpentinized [Kelemen et al. 2020] and cannot be used directly to correlate with
141 seismic observations. On the other hand, the observation of core complexes and serpentinized
142 peridotite on the seafloor has led to the suggestion that the lower crust consists of serpentinized
143 peridotite and the Moho could represent a serpentinization front [Cannat, 1993].
144



145
146 **Figure 2: MTZ in Oman Ophiolite:** The ophiolite section from the Oman region, where layered gabbro of
147 lower oceanic crust and mantle harzburgite are separated by dunite layer of the Moho Transition Zone
148 (MTZ). Insets show examples of the different geology around the MTZ, such as wehrlite, layered gabbro,
149 gabbro sills within the MTZ and banded dunite from the upper mantle.

150
151 In conclusion, the Moho could either be a sharp boundary or could be a thick transition
152 zone, depending upon the physical and chemical processes that have created it. For example, as the
153 melt migrates (percolates) from the mantle towards the surface to form the magmatic part of the
154 crust, it would interact and react with host rocks, creating a complex heterogeneity within the MTZ

155 depending upon different physical and chemical conditions [Boudier and Nicolas, 1995]. For
156 example, in the Bay of Islands ophiolite, the MTZ consists of a combination of gabbroic sills,
157 wehrlite, dunite and harzburgite [Collins et al. 1986]. Furthermore, the MTZ is also influenced by
158 the mantle flow and ductile deformation beneath the ridge axis [Boudier and Nicolas, 1995]. In
159 other words, the MTZ acts as a physical and chemical filter separating the crust above from the
160 mantle below. In any case, at a sharp Moho, the change in the P-wave velocity would be abrupt and
161 could be interpreted as a rapid change from mafic crustal composition to ultra-mafic mantle
162 composition [Karson et al. 1984]. In a thick MTZ, there could be a smooth P-wave velocity gradient
163 representing a gradual transition from mafic to ultra-mafic compositions or a layering with low and
164 high velocities of gabbroic and mantle rocks, which might be the case for slow or ultra-slow
165 spreading crust [Kempner and Gettrust, 1982].

166

167 The synthetic seismogram modelling study for velocity models derived from seismic
168 reflection or refraction data [Helmberger and Morris, 1969; Fuchs and Muller, 1971; Fowler and
169 Keen, 1979] and from ophiolites [Kempner and Gettrust, 1982; Brocher et al. 1985; Collins et al.
170 1986; Brocher and Frazer, 1987] have been carried out using ray-tracing [Helmberger and Morris,
171 1969] and reflectivity [Fuchs and Muller, 1971] methods. Brocher et al. [1985] computed normal
172 incidence synthetic seismograms for 1D velocity models for the Oman and the Bay of Islands
173 ophiolites while Collins et al. [1986] extended this study to 2D velocity models to characterise near
174 offset seismic reflection response from the Moho in the Bay of Islands ophiolite. These studies were
175 further extended to wide-angle Ocean-Bottom Seismometer (OBS) geometry to understand the
176 nature of both seismic reflection and refraction arrivals [Spudich and Orcutt, 1980; Sereno and
177 Orcutt, 1985; Jarchow and Thompson, 1989; Prodehl et al. 2013]. A similar study was performed
178 for continental Moho [Carbonell et al. 2002]. However, the variations in lower crustal and upper
179 mantle structures on the reflection characteristics from Moho have not been examined in detail
180 [Mutter and Carton, 2013]. For example, there are no detailed studies showing the dependence of
181 the lower crust velocity models on the nature of Pg arrivals, interaction of the lower crustal arrivals
182 with PmP arrivals near critical distance and the changes in the nature of PmP reflection both at near
183 offset and at far offsets due to structural variations in MTZ. Also, the amplitude versus offset
184 (AVO) analysis of PmP reflection arrivals, which provides significant information on the
185 characteristics of MTZ, has never been attempted. Here we have performed the AVO analysis for
186 different thicknesses and geometries of MTZ to understand the variation in AVO response. We
187 present a comprehensive synthetic seismogram study that includes small scale variations in the
188 lower crust and MTZ to get insight about the role of the various structural features on amplitude and
189 phase covering a wide range of offsets from 0 to 45 km allowing to analyse all the arrivals in detail.
190 We also show why and how the conventional full waveform inversion techniques [Shipp and Singh,

191 2002] will have difficulties in resolving the finer details of reflection from Moho near critical
192 distance from OBS data, and propose a solution for designing seismic experiments and inversion
193 strategies to understand the nature of the lower crust and MTZ.

194

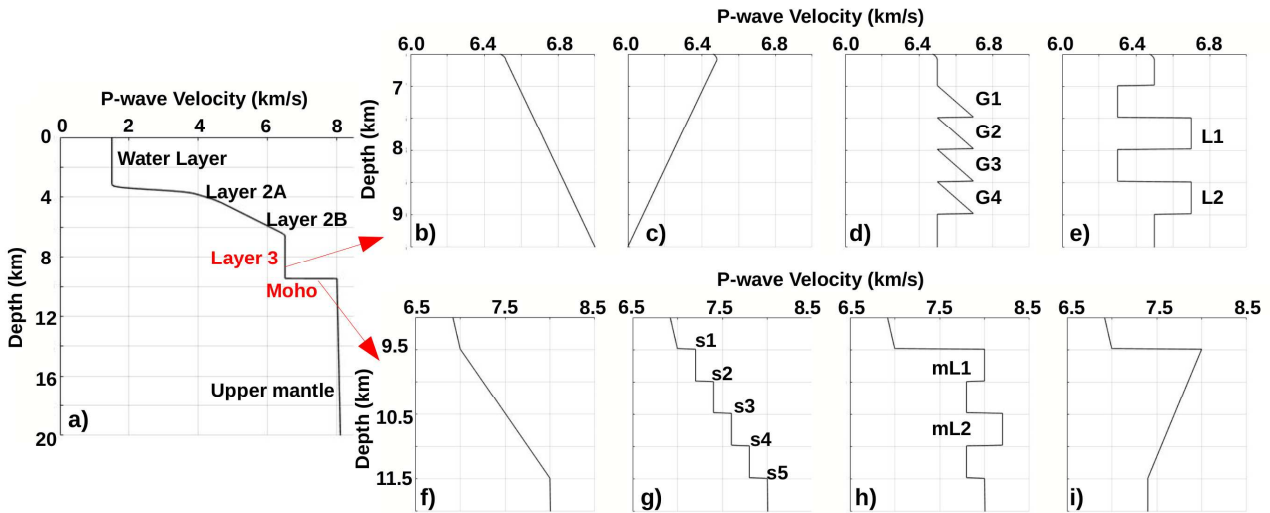
195 **2 Velocity Models**

196 We have constructed one-dimensional (1D) models based on a three-layer generic slow-
197 spreading oceanic crustal model [e.g. White et al. 1992] where the crust is 6 km thick. We assume a
198 water depth of 3.5 km. The P-wave velocity at the seafloor increases from 3.5 km/s to 4.5 km/s in a
199 700 m thick zone, representing Layer 2A [Grevemeyer et al. 1998; Audhkhasi and Singh, 2019],
200 followed by a linear increase in velocity from 4.5 km/s to 6.5 km/s in a 2300-m thick zone
201 representing Layer 2B, and a 3-km thick Layer 3 (lower crust). The Moho boundary lies at 9.5 km
202 depth and the mantle extends down to 20 km (bottom of the velocity model). The ratio of P and S
203 velocities was approximated as 1.73 [Shipp and Singh, 2002], assuming a Poisson ratio of 0.25
204 [Collier and Singh, 1998].

205

206 We have kept the upper crustal velocity fixed and varied only the velocity in the lower crust
207 and at the MTZ. Five different velocity models are created by changing velocities in the lower crust
208 (Figure 3). These models include the lower crust with a constant velocity (Figure 3a), a positive
209 velocity gradient (Figure 3b), a negative velocity gradient (Figure 3c), a gradational velocity
210 layering (Figure 3d) and a layered velocity model (Figure 3e). In the constant velocity model, the
211 velocity in the lower crust is 6.5 km/s. In the positive gradient velocity model (Figure 3b), the
212 velocity increases linearly from 6.5 km/s (top of the lower crust) to 7 km/s (bottom of the lower
213 crust) at 9.5 km depth with a velocity gradient of 0.17 s^{-1} . The smaller velocity gradient of 0.17 s^{-1}
214 compared to a higher velocity gradient in the upper crust ($\sim 1.1 \text{ s}^{-1}$) could be due to minute
215 petrological variations, metamorphic changes, the effects of pressure and temperature at lower
216 crustal depths [White et al. 1992; Christenson et al. 2019]. On the other hand, in the negative
217 velocity gradient model (Figure 3c), the velocity decreases linearly from 6.5 km/s to 6.0 km/s with a
218 velocity gradient of -0.17 s^{-1} . The negative velocity gradient in the lower crust could be the result of
219 a progressive serpentinization of upper mantle material to crustal velocity material [Mithal and
220 Mutter, 1989]. In the gradational velocity model (Figure 3d), the velocity in the lower crust consists
221 of four layers (G1, G2, G3 and G4), where the velocity in each layer increases linearly by 200 m/s
222 in a 500 m thick zone, with a sharp boundary at the base where the velocity decreases to 6.5 km/s
223 (background velocity). In the layered velocity model (Figure 3e), there are four 500-m thick layers
224 each with constant velocities of $\pm 200 \text{ m/s}$ from the background velocity of 6.5 km/s, representing a
225 layered lower crust. Two high velocity layers are marked as L1 and L2. The gradational and layered
226 velocity models could represent oceanic layered gabbro [Schanker and Lippsett 2016; Jousset et

227 al. 2012] which could have occurred due to hydrothermal alteration in the lower crust [Singh et al.
 228 1999] or the lower crust could have been formed by in situ cooling and crystallisation of melt sills
 229 in the lower crust (sheeted sill model) [Kelemen et al. 1997]. In both gradational and layered
 230 models, the topmost and bottommost parts of the lower crust are 500 m thick with a velocity of 6.5
 231 km/s.
 232



233
 234 **Figure 3: Velocity Models:** a) 1D generic velocity model of oceanic crust and upper mantle, showing
 235 different layers such as water layer, Layer 2A, 2B of upper oceanic crust, Layer 3 (lower oceanic crust),
 236 Moho boundary and upper mantle. The upper panel represents four variants of the lower crust velocity
 237 structure, namely b) positive velocity gradient, c) negative velocity gradient, d) gradational layering with 4
 238 layers G1, G2, G3 and G4, and e) layered velocity where two high-velocity layers are marked as L1 and L2.
 239 The bottom panel represents four variants of the MTZ, namely f) gradient MTZ, g) staircase MTZ with 5
 240 steps; s1, s2, s3, s4 and s5, h) layered MTZ, where two high velocity layers are marked as mL1 and mL2,
 241 and i) low velocity beneath a sharp MTZ.

242
 243 Different types of MTZ models are assumed below the lower crust where the velocity in the
 244 mantle (below MTZ) is assumed to be 8 km/s, which increases linearly to 8.1 km/s at the bottom of
 245 the model at 20 km depth. A sharp Moho is defined as an interface where the velocity increases
 246 from 7 km/s to 8 km/s (Figure 3a) [Foulger et al. 2003]. A thick MTZ can have a linear velocity
 247 gradient of different thicknesses or can have layered structures. At the sharp boundary, the P-wave
 248 velocity shows an abrupt transition and could be interpreted as a rapid change from mafic crustal
 249 composition to ultra-mafic mantle composition [Karson et al. 1984]. In the thick layer MTZ, there is
 250 a linear gradient of P-wave velocity representing the gradual transition between mafic and ultra-
 251 mafic compositions [Collins et al. 1986]. For the gradient MTZ, the velocity increases linearly from
 252 7 km/s to 8 km/s from 9.5 km to 11.5 km depth, in a 2 km thick gradient zone (Figure 3f). The MTZ
 253 could have a staircase Moho structure, where the velocity increases by 200 m/s at every 500 m in

254 the MTZ of 2 km thickness (Figure 3g), representing five steps; s1, s2, s3, s4 and s5. The gradient
255 and staircase Moho could represent MTZ for slow spreading crust [White et al. 1992; Ohira et al.
256 2017]. Sometimes, there could be banded dunites, gabbro sills or a number of parallel and
257 horizontal gabbro lenses [Boudier and Nicolas, 1995] just below the Moho, which would produce a
258 layered MTZ. In the layered MTZ model (Figure 3h), the velocity increases from 7 km/s to 8 km/s
259 at the Moho interface at 9.5 km depth and then there are three 500 m thick alternating low and high-
260 velocity layers (mL1 and mL2) with a velocity of change of ± 200 m/s over the background velocity
261 of 8 km/s, representing the banded dunite layering in harzburgite [Dick and Sinton, 1979; Karson et
262 al. 1984] or the presence of a number of gabbro sills in the MTZ [Boudier and Nicolas, 1995]. At
263 the gabbro-harzburgite boundary the velocity variations would be much larger, from 6.7 km to 8.1
264 km/s.

265

266 For a P-wave velocity of 6.5 km/s to 8 km/s and a dominant frequency of 5-10 Hz, the
267 wavelength will be between 650 m and 1600 m, and therefore, a 500 m layer thickness is reasonable
268 in order to resolve these layers using seismic methods, such as seismic full waveform inversion
269 [Guo et al. 2021a]. It is possible that layers could be thinner, but we cannot resolve them using
270 current OBS types of data, and therefore we have not considered thinner layers. However, a stack of
271 thin layers in the lower crust, as observed in the Oman ophiolite, would lead to anisotropy [Backus,
272 1962], which should be taken into account during data analysis. To resolve these layers, higher
273 frequency data would be required. In the last model (Figure 3i), velocity decreases from 8 km/s to
274 7.4 km/s over a 2 km thick layer below the sharp Moho, which remains at 7.4 km/s to the base of
275 the model, representing a low-velocity layer in the upper mantle. Though there are large structural
276 variations observed from the lower crust and MTZ using wide-angle studies [White et al. 1992],
277 there is a lack of focused study on seismogram modelling for such variations present in the oceanic
278 crust. In our study, we collectively use these different velocity models of the oceanic crust to
279 understand the differences in seismic response of the different arrivals.

280

281 **3 Methodology**

282 **3.1 Forward Modelling**

283 In our study, we have used a finite-difference solution of the elastic wave equation in the
284 time and space domain [Levander, 1988] to compute synthetic seismograms. The finite difference
285 method is capable of modelling any type of waves including refracted waves, turning waves,
286 interbed multiples and converted waves and hence it helps to accurately model complex seismic
287 wavefields. We use elastic modelling to make sure that the energy partitioning between P- and S-
288 waves at interfaces is properly taken into account. This is specifically important for modelling of
289 wide-angle reflections where the P-to-S partitioning is significant. The grid for the finite-difference

290 scheme is staggered both in time and space. This helps to generate second-order time operator and
291 fourth-order spatial operator. It requires only five grid points per wavelength to minimise the grid
292 dispersion which is computationally less intensive. For this synthetic seismogram modelling, we
293 have used the algorithm developed by Shipp and Singh [2002]. The primary inputs for the synthetic
294 seismogram modelling are: P- and S-wave velocity models, density, a source wavelet, the source-
295 receiver geometry, and the boundary conditions. We have applied the optimal absorbing boundary
296 conditions to attenuate the artefacts in the synthetic seismogram from the boundaries of the medium
297 [Peng and Toksöz, 1995] so that there are no reflections or conversions from the boundaries.

298

299 **3.2 Source and Receiver Configuration**

300 For near-offset and wide-angle geometry, we have used an offset range of 0 to 45 km. For
301 1D modelling, we have used single source and multiple receivers at 10 m (one grid point: same used
302 for designing 1D velocity model) interval, allowing the simulation of multichannel seismic data.
303 The source is located at 50 m within the model. The five grid points before the source and after the
304 last receiver are kept empty and we have applied optimal absorbing boundary conditions to avoid
305 artefacts (like reflections or conversions) from the boundary of the model. The length of the
306 streamer is designed to ensure that all types of waves (Pg, PmP, Pn) from the deepest parts of the
307 model can be recorded. For the source wavelet, we have used a Ricker wavelet, with a dominant
308 frequency of 10 Hz. According to stability criteria (grid spacing and a maximum frequency of
309 source), the time step increment (t) is 0.0007 s and the total number of time steps per trace is 19000
310 so that we are able to obtain travel time data of ~14 s, which is sufficient to obtain the seismograms
311 for arrivals from the end of the model.

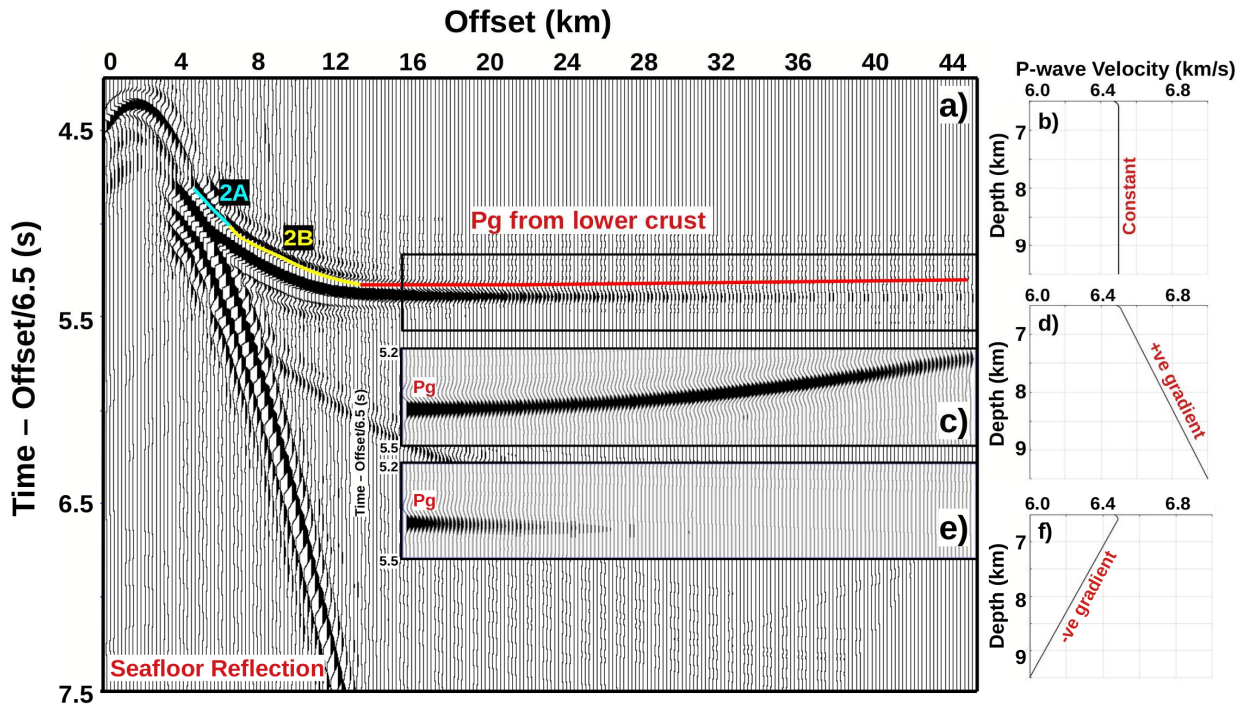
312

313 **4 Results**

314 **4.1 Lower Crust Models**

315 We first modelled a constant velocity, a positive velocity gradient and a negative velocity
316 gradient in the lower crust without Moho interface. The synthetic seismograms for the constant
317 velocity lower crustal model (Figure 4b) for the whole offsets (0-45 km) are shown in Figure 4a.
318 Here we have plotted true amplitude (without normalisation) synthetic seismograms with offset as a
319 horizontal axis and travel time as a vertical axis with an apparent reduction velocity of 6.5 km/s. We
320 observed two primary seismic arrivals: the reflection from the seafloor and the P turning rays (Pg)
321 from the upper crust. Here, the arrivals between 4-6 km correspond to Layer 2A. Between 6 and 14
322 km offset, we observe arrivals from Layer 2B. As these two rays are turning rays, they have large
323 amplitudes with an apparent velocity corresponding to their respective velocities in these layers. At
324 offset >14 km, we observed refraction arrivals with an apparent velocity of 6.5 km/s, which occur
325 due to the velocity change from Layer 2B to Layer 3. The amplitude of these arrivals slowly

326 decreases with the increase in offset. For the positive velocity gradient (Figure 4d) in the lower
 327 crust (Figure 4c), the amplitude of the Pg arrival continues to be large at far offsets and it travels
 328 with increasing (6.5 km/s to 7 km/s) apparent velocities. In contrast, for the negative velocity
 329 gradient (Figure 4f), the amplitude of the arrivals decreases rapidly with offset and is not observed
 330 beyond 28 km offset (Figure 4e). So the presence of a strong Pg arrival at far offsets would indicate
 331 the existence of a positive velocity gradient layer in the lower crust and a weak Pg arrival at far
 332 offsets is suggestive of a low velocity gradient in the lower crust.
 333

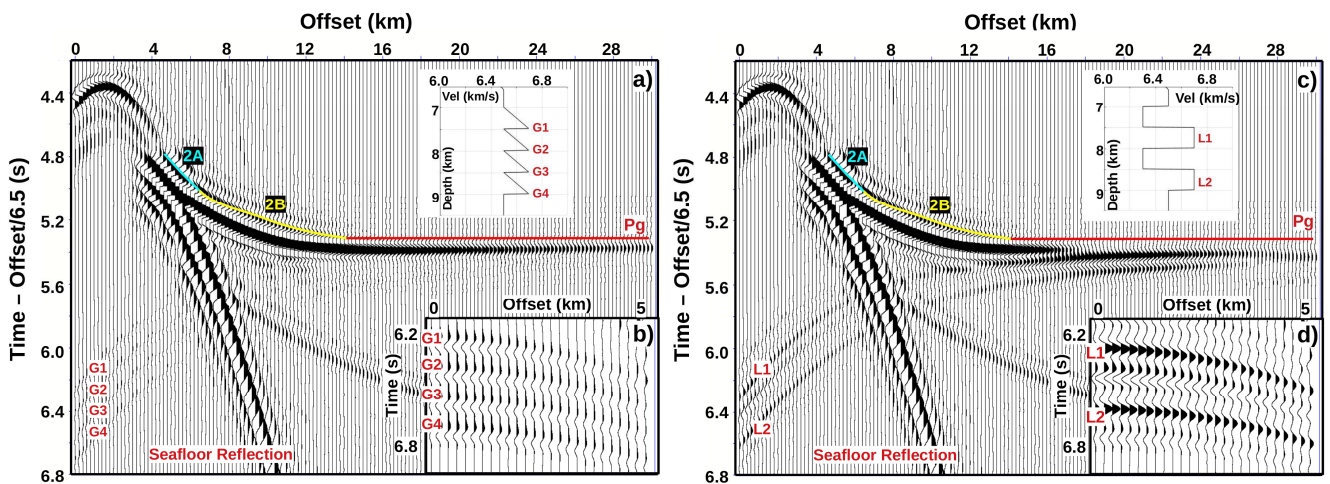


334
 335 **Figure 4: Synthetic Seismograms for simple models in the lower crust without Moho:** a) Whole offset
 336 (0-45 km) synthetic seismograms for the generic velocity with a constant velocity in the lower crust , as
 337 shown in b), without Moho showing the seafloor reflection and the Pg arrivals from Layer 2A (cyan color),
 338 2B (yellow color) and lower crust (red color). The vertical axis is the reduced time with a reduction velocity
 339 of 6.5 km/s and the horizontal axis is the source-receiver offset in km. In the 2 insets, the Pg wave is
 340 extracted in the offset range of 16-45 km; c) for the positive gradient velocity model, as shown in d) and e)
 341 for the negative gradient velocity model, as shown in f).
 342

343 When we compute synthetic seismograms for the gradational velocity model in the lower
 344 crust, we observed four low-amplitude, low-and-high frequency reflections (G1, G2, G3 and G4)
 345 starting at zero offset up to \approx 6 km offset, before seafloor reflection arrival (Figure 5a). The low-
 346 frequency part of the reflected energy is due to the linear increase in velocity in the 500-m thick
 347 zone, and the high-frequency signal is due to the sharp decrease in velocity (-200 m/s) at the base of
 348 the layer (Figure 5b). The amplitude and the time difference between these reflections decrease with
 349 the increase in offsets. As the velocity variations at the base of these layers are small, the velocity

350 contrast is small (0.03) as compared to the Moho reflection which could be ~ 0.12 . As the offset
 351 increases, the arrivals from different layers interfere and cancel out and hence do not affect the Pg
 352 arrivals at far offset much. However, the amplitude of the Pg arrival is slightly higher than those for
 353 the constant velocity layer due to an increase in the average P-wave velocity in the lower crust. For
 354 the layered lower crustal model, we observe alternate negative and positive polarity reflections,
 355 starting at zero offset (Figure 5c,d). We have marked the positive polarity reflections as L1 and L2,
 356 which can be followed up to 8-24 km offset as they merge with the Pg arrivals. The change in the
 357 polarity corresponds to alternate layers of the low and high velocities with respect to the
 358 background velocity of 6.5 km/s in the lower crust. Because of the high-velocity contrasts and
 359 interference effects, one can observe strong wide-angle reflections between 12 and 17 km offset
 360 from L1, which interfere with the Pg arrival, and the second wide-angle reflections at 16-24 km
 361 offsets. The shingling effect is observed at 17-18 km offset due to the first low velocity layer. These
 362 observations suggest that Pg arrivals are sensitive to layered structures in the lower crust, which has
 363 been independently confirmed by Guo et al. [2021a]. At zero offset, the amplitudes of these
 364 secondary reflection arrivals (L1 and L2 in Figure 5d) for the layered lower crust having alternate
 365 high and low velocity layers are higher than the amplitudes G1 to G4 for the gradational lower
 366 crust having velocity increasing in steps (Figure 5b) because of the high-velocity contrast in the
 367 layered lower crust, i.e., 400 m/s over 200 m/s for the gradational model.

368



369

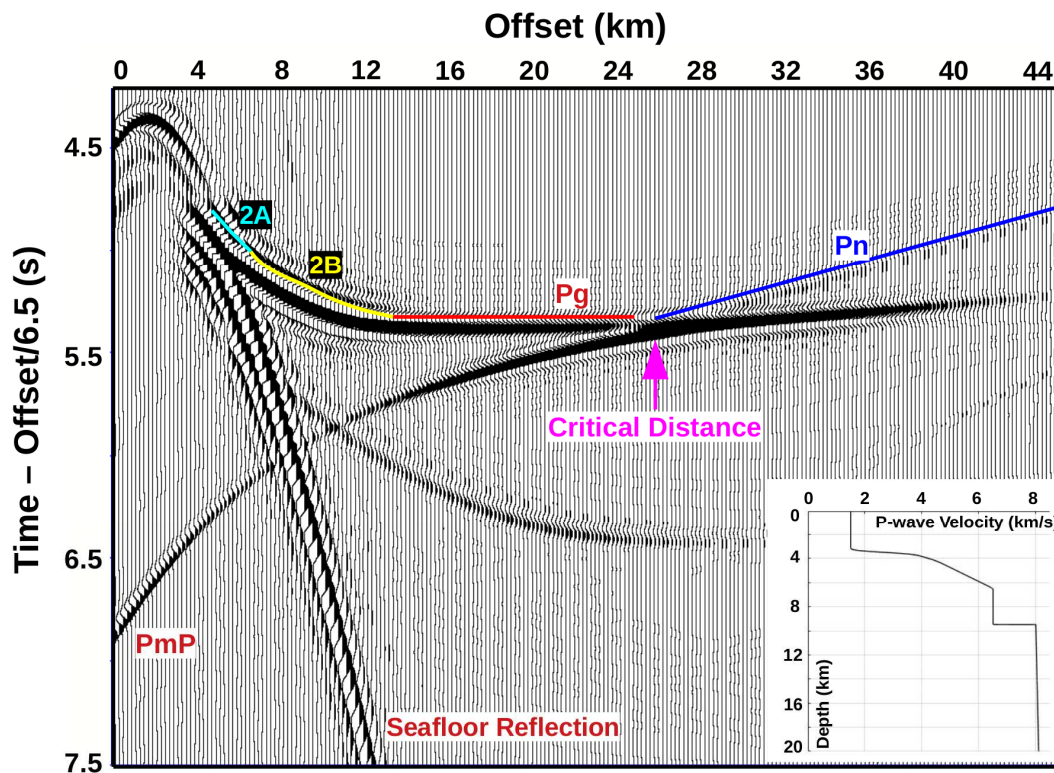
370 **Figure 5: Synthetic seismograms for layered structures in the lower crust without Moho: a)** Whole
 371 offset (0-45 km) synthetic seismogram for the gradational lower crustal velocity model, as shown in the
 372 upper inset. Seismic phases are the same as described in Figure 4. In the synthetic seismograms, phases G1,
 373 G2, G3 and G4 mark the low-amplitude reflections due to the gradational layering in the velocity model. **b)**
 374 Enlarged portion of the lower crustal reflections (G1-G4) at near offset (0-5 km) plotted without any
 375 reduction velocity. **c)** Synthetic seismogram for layered velocity model, as shown in the upper inset; L1 and
 376 L2 mark the positive polarity reflections due to layering in the velocity model. **d)** Enlarge portion of the two
 377 lower crustal reflections (L1 and L2) plotted without any reduction velocity.

378

379 4.2 Lower Crust Models and a Sharp Moho

380 Having the information about the waveform of Pg for a suite of five different lower crust
381 velocity models, we now analyse the effect of these lower crustal models on the reflection arrival
382 (PmP) from the Moho. For this, we have introduced a sharp Moho boundary in all five models of
383 the lower crust at 9.5 km depth. The whole offset (0-45 km) synthetic seismograms for the positive
384 gradient velocity model with a sharp Moho is shown in Figure 6. Other than seafloor reflection and
385 Pg arrivals, we observe a strong PmP reflection over the entire length of offset. The Pn refraction
386 from the mantle is observed after the critical distance at 26 km (distance at which PmP has
387 maximum amplitude). The Pn arrival is tangent to the PmP arrival at the critical distance. As the Pn
388 is a head wave, its amplitude decreases rapidly with offset. Also note that the Pg arrivals at
389 offsets >26 km are no more independent, but have merged with the PmP arrivals.

390



391

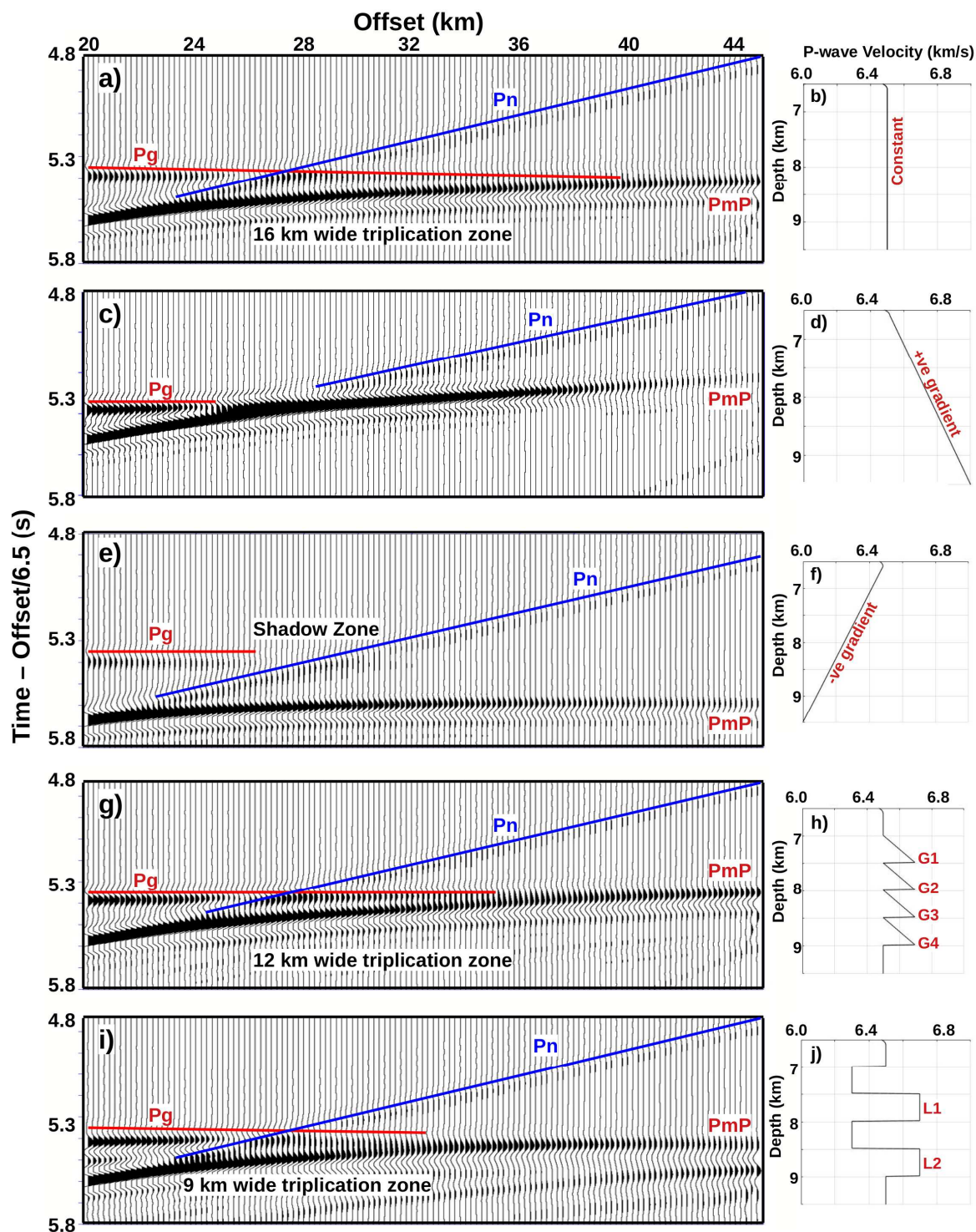
392 **Figure 6: Seismogram for a positive velocity gradient lower crust with a sharp Moho:** Whole offset (0-
393 45 km) synthetic seismogram for the positive velocity gradient with a sharp Moho boundary, as shown in the
394 inset. Other than the seafloor reflection and crustal Pg arrivals, the PmP reflection starts at zero offset and Pn
395 (marked in blue) arrival starts after the critical distance. Note the large amplitude wide-angle PmP reflections
396 starting from 14 km offset and extending up to 38 km offset, with the critical offset at 26 km offset,
397 representing a typical wide-angle seismic data in the oceanic domain. Both Pg and Pn arrivals are tangent to
398 PmP arrival at the critical distance.

399

400 Except for the waveform of PmP in synthetic seismograms for the sharp Moho below
401 different lower crust models, all the rest of the features are similar, as shown in Figure 4 or Figure 5
402 and therefore, the whole offset synthetic seismograms for the remaining four models (constant,
403 negative gradient, gradational and layered velocity) are shown in the supplementary Figure S1.

404

405 Figure 7 shows wide-angle data (20-45 km) for all five models of the lower crust with a
406 sharp Moho. A clear triplication zone encompassed by the Pg, Pn and PmP arrivals is observed for
407 the constant lower crustal velocity (Figure 7b) model over 16-km offset range (Figure 7a). The
408 offset range for the triplication zone (width) is defined by the offset at which Pg and Pn become
409 tangent respectively to PmP. For the positive velocity gradient model (Figure 7d), the extent of
410 velocity contrast between the lower crust and the Moho boundary decreases and the triplication
411 reduces to a point at 27 km offset (Figure 7c) where the Pg interferes with the PmP just before the
412 critical distance. On the other hand, the presence of a negative velocity gradient in the lower crust
413 (Figure 7f) generates a shadow zone with a clear time shift between the PmP and Pg arrivals; the
414 triplication disappears, and the Pg extends only up to Pn arrival (Figure 7e). The PmP is a clean
415 arrival without any interference with Pg arrival. For the gradational (Figure 7h) and layered lower
416 crust (Figure 7j) models, we observe a triplication similar to the constant velocity model, but here
417 the width of the triplication zone (lateral extent) is 12 km for the gradational velocity model (Figure
418 7g) and 9 km for the layered velocity model (Figure 7i). This decrease in the width of the
419 triplication zone is the result of a slightly increased average P-wave velocity in the lower crust and
420 the interference of small amplitude reflections with Pg arrival. The difference in the width of these
421 triplication zones for the gradational and layered lower crust is the result of the amplitudes of G1 to
422 G4 and L1, L2 reflections. This means that the interference of low amplitude reflections (G1 to G4)
423 with Pg changes its waveform to a smaller extent as compared with the interference of high
424 amplitude reflections (L1 and L2) with Pg. At far offsets, we also observe interbed multiples below
425 the PmP arrival for the layered lower crustal (Figure 7i). Because of the interference of lower
426 crustal reflections with PmP at the end of the triplication zone, the amplitude of the PmP reflection
427 at far offsets (> 40 km) is high except for the positive and negative velocity gradients in the lower
428 crust. But the PmP amplitude is lower for the positive velocity gradient as compared with the
429 negative velocity gradient because the former has a low-velocity contrast between the lower crust
430 and the sharp MTZ than the latter.



431

432 **Figure 7: Wide-angle arrivals for the lower crust models with a Moho boundary:** Wide-angle (20-45 km
 433 offset) synthetic seismograms for five lower crustal models when there is a sharp Moho boundary at the
 434 bottom of the lower crust. **a)** A 16-km-wide triplication zone between Pg, PmP and Pn for the constant
 435 velocity in the lower crust, as shown in **b)**. **c)** The absence of a triplication for the positive velocity gradient
 436 model, as shown in **d)**. **e)** A shadow zone above the PmP arrival for the negative velocity gradient model, as
 437 shown in **f)**. **g)** A 12-km-wide triplication zone for the gradational velocity model, as shown in **h)**, and **i)**
 438 a 9-km-wide triplication zone for the layered velocity model, as shown in **j)**. Note the interbed multiples below
 439 the PmP arrivals for the layered velocity model.

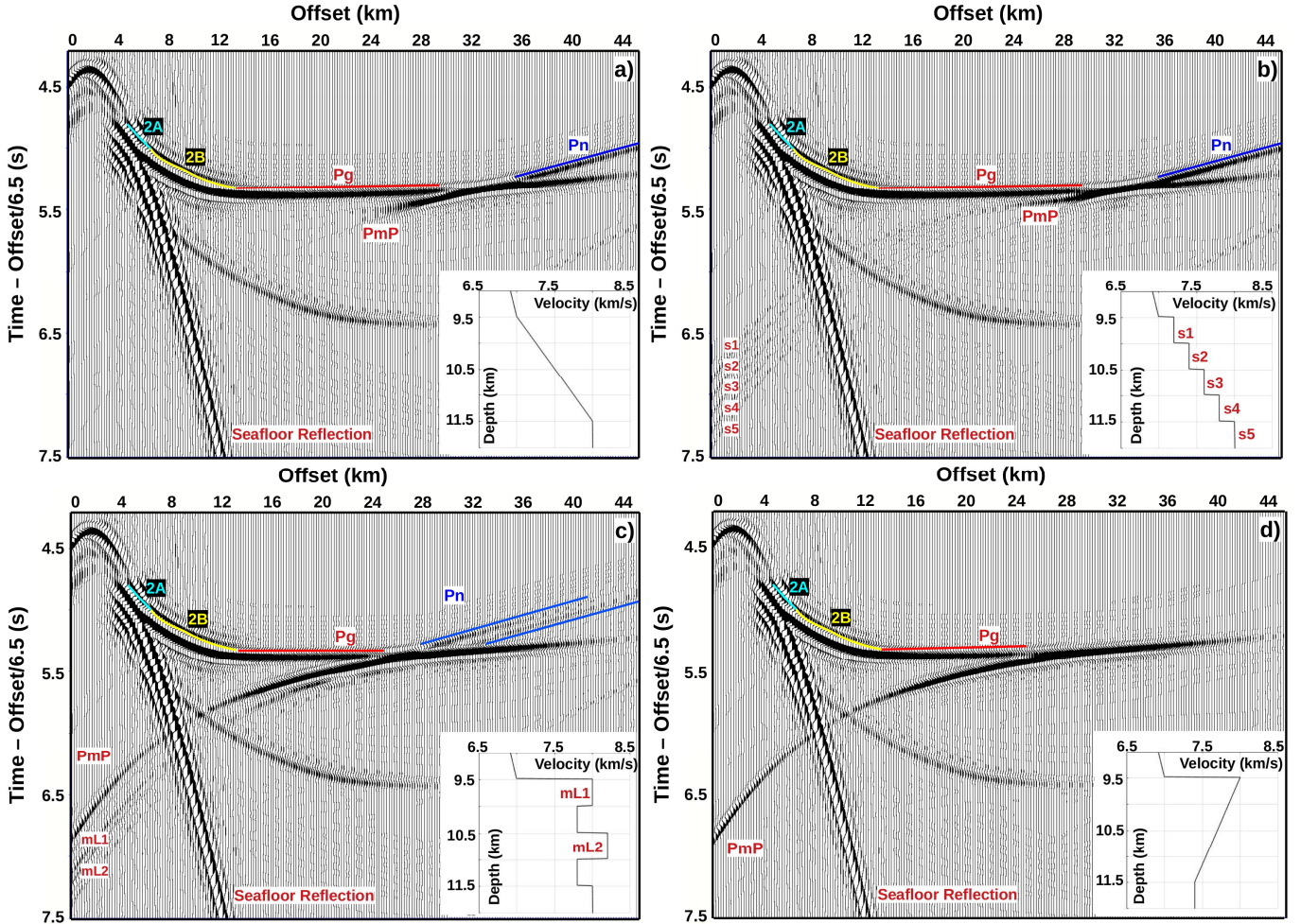
440

441 4.3 Moho Transition Zone Models

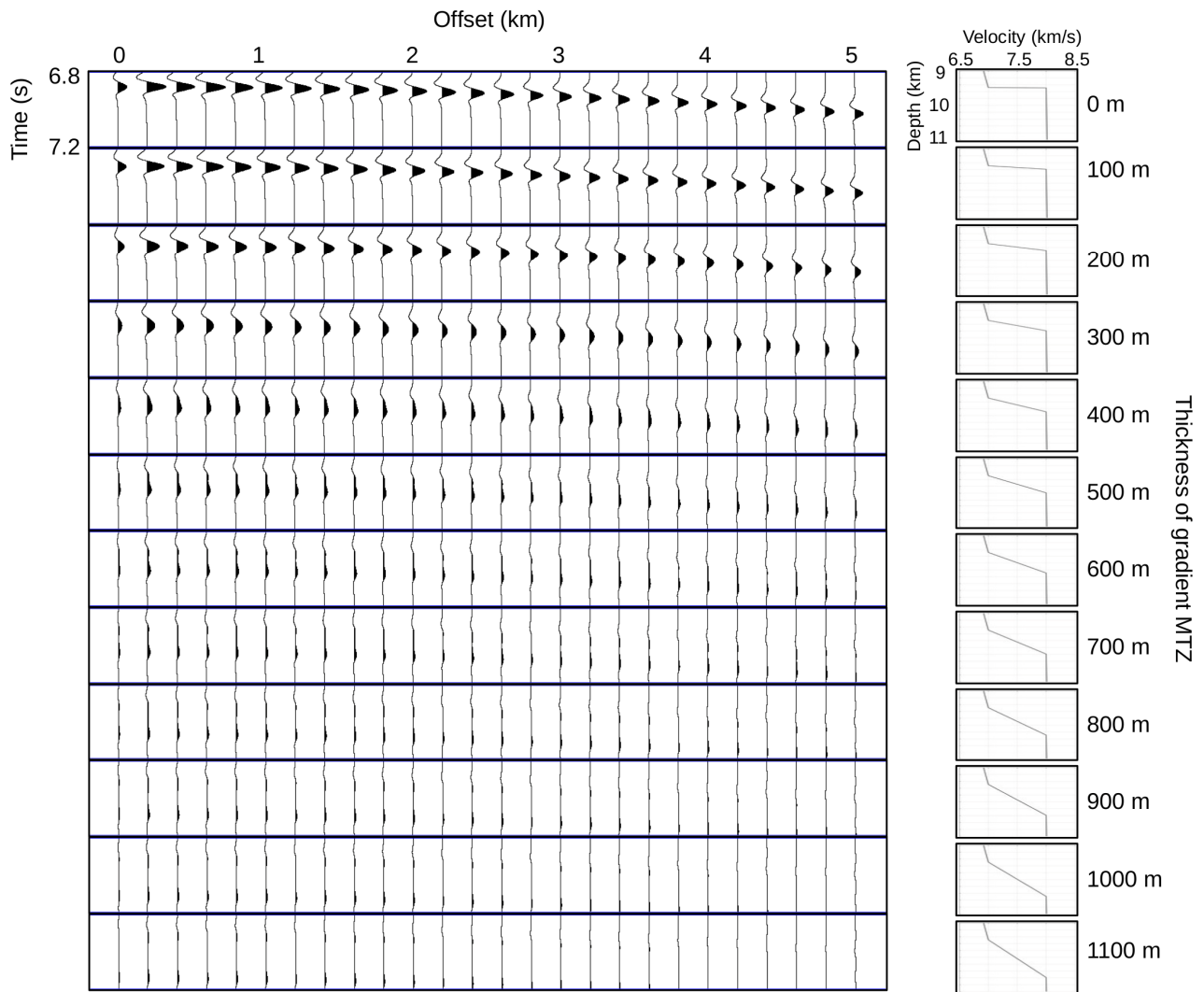
442 The synthetic seismogram for a sharp MTZ with a positive velocity gradient in the lower
443 crust represents the typical reflection response from the Moho (Figure 6). On the other hand, when
444 the MTZ becomes a 2000 m thick gradient zone, the PmP arrival does not start at zero offset but at
445 22 km offset (Figure 8a), and there is no triplication. Here the critical distance is ~ 33 km, instead of
446 26 km for the sharp Moho. To understand the relation between the waveform of the PmP arrival and
447 the gradient MTZ thickness, we varied the thickness of the gradient zone from 0 m to 2000 m over a
448 step of 100 m (Figure 9 and S2). When the MTZ thickness increases from 0 m to 300 m, the
449 amplitude of the Moho reflection at near offsets (0-5 km) does not change much (Figure 9). When
450 the MTZ thickness increases up to 1000 m, the amplitude decreases gradually and the waveform
451 widens, resulting in the diffusion of reflection from the MTZ (Figure 9). When the thickness
452 reaches 1100 m, the PmP reflection is not observed at zero offset (last panel of Figure 9). These
453 results of diffused Moho reflections are consistent with the results obtained by Ohira et al. [2017],
454 where the zero-offset data show weak amplitude or absence of reflection from the Moho when the
455 thickness of the MTZ is ~ 1 km. When the thickness of the MTZ is greater than 1100 m, the offset at
456 which PmP is observed increases with the increasing MTZ thickness (Figure S2), and the maximum
457 amplitude of the PmP arrival also increases. The critical distance linearly increases with the
458 thickness of MTZ, i.e. by ~ 350 m for every 100 m increase in the MTZ thickness (Figure 10). To
459 calculate the critical distance, here we have used the locally maximum amplitude of the PmP arrival
460 where the Pn arrival is tangent to the PmP. Thus the location of the critical distance can be used to
461 get some idea about the nature of the MTZ. Furthermore, large amplitude PmP arrivals can be
462 observed at broad far offset range in the presence of a sharp Moho whereas in the presence of a
463 thick MTZ, the offset extent of the PmP arrivals lies within a limited offset range around the critical
464 distance. Note that we have used the term critical distance in a more generic sense, not *sensu stricto*
465 where the term critical distance is defined for a sharp high velocity contrast.

466
467 In the case of the staircase MTZ model, five weak reflections at zero offset are observed (s1-
468 s5), because of the increase in the velocity by 200 m/s over the steps of 500 m thick zone (Figure
469 8b). The amplitudes of s2, s3, s4 and s5 reflections decrease as the offset increases. The amplitude
470 of s1 slightly increases after 21 km offset and merges with the PmP reflection at 29 km offset. All
471 the other reflections (s2-s5) also merge with this event (PmP) as the offset increases. The critical
472 distance occurs at 34 km offset, similar to the 2-km thick velocity gradient model (Figure 8a), and
473 therefore, it would be difficult to distinguish between a gradient MTZ and a staircase MTZ only
474 from the arrival times of wide-angle seismic data. However, the waveforms are different, and hence
475 a full waveform inversion type approach should allow to distinguish a linear gradient MTZ from a
476 staircase MTZ. In the case of a layered Moho (Figure 8c), there are small-amplitude reflection

477 arrivals below the PmP reflection (marked as mL1 and mL2) due to the alternate low and high
 478 velocity layers over the background velocity of 8 km/s below the sharp MTZ. The amplitude of
 479 mL1 is higher than mL2 because of the difference in the velocity contrast. The mL2 reflection is not
 480 observed after 8 km offset and mL1 reflection merges with the PmP arrival at 21 km offset.
 481

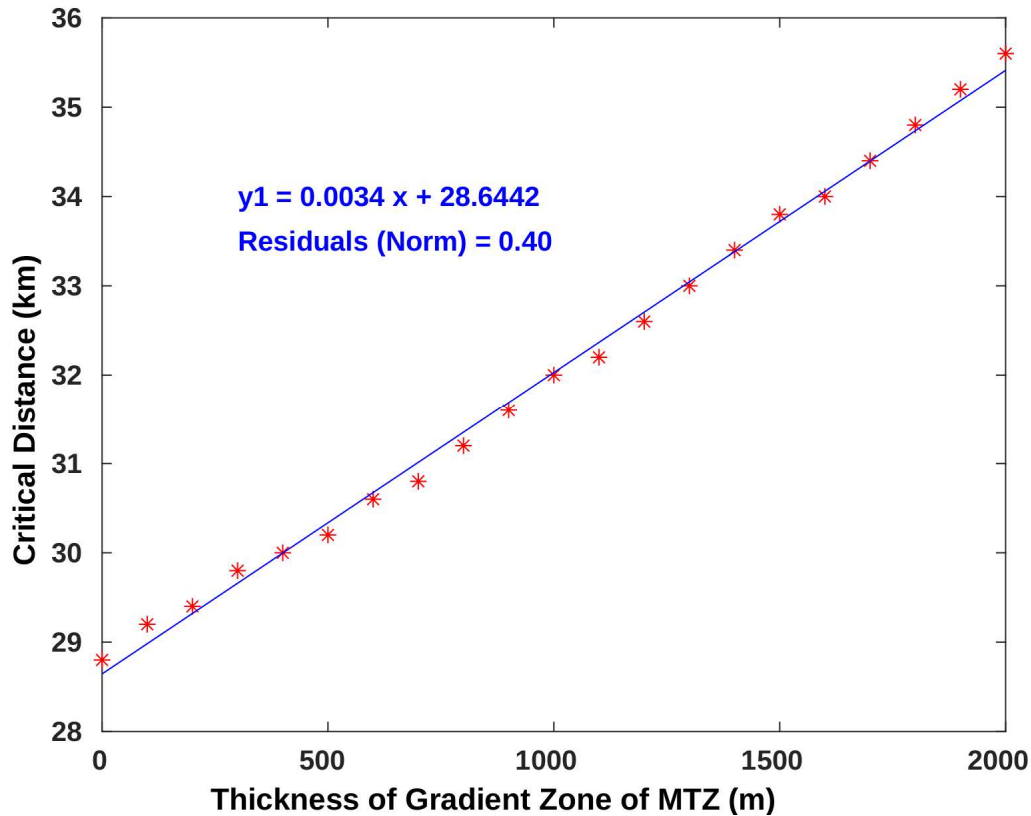


482
 483 **Figure 8: MTZ Seismograms:** Whole offset (0-45 km) synthetic seismograms for different MTZ models. **a)**
 484 Seismogram for the gradient MTZ velocity model, containing PmP arrivals starting at 22 km offset. **b)**
 485 Seismogram for the staircase MTZ contains low amplitude reflections s1, s2, s3, s4 and s5 starting at zero
 486 offset and strong PmP starting at 23 km offset. **c)** Seismogram for the layered MTZ; besides PmP, two low-
 487 amplitude reflections (mL1, mL2) start at zero offset, and the Pn becomes a multi-phase arrival (marked by
 488 two blue lines). **d)** Seismogram for a low velocity layer beneath the sharp MTZ indicating the absence of Pn
 489 arrivals. The respective velocity models are shown as insets at the bottom right of each seismogram.
 490



491
 492 **Figure 9: Near offset reflections for a gradient MTZ:** Near offset (0-5 km) synthetic seismograms
 493 showing only the PmP reflection for different thickness of the gradient MTZ with thickness varying 0 m to
 494 1100 m, as shown on the right side of the figure. The velocity models for different thicknesses of gradient
 495 MTZ are shown only between 9-11 km depth. The numbers on the right of the velocity models indicate the
 496 thickness of the gradient MTZ. In the seismograms, the time axis is plotted without any reduction velocity in
 497 a 400 ms window (6.8-7.2 s) encompassing the Moho reflections in all panels.

498
 499 Furthermore, we observed that the Pn refraction is a single phase arrival for the sharp,
 500 gradient and staircase MTZ models, but it becomes multiphase, one starting at 28 km offset and the
 501 second one at 32 km, due to the presence of alternate high and low velocity layers below the sharp
 502 MTZ (Figure 8c). So, the presence of high and low velocity layers below the MTZ does not only
 503 produce reflections starting at zero offset (below PmP) but also changes the signature of Pn
 504 refraction. Therefore, the waveform coda of the PmP and Pn arrivals should provide information
 505 about the layered MTZ. Finally, when the velocity in the mantle becomes < 8 km/s, we do not
 506 observe Pn refraction after critical distance (Figure 8d), which means decreasing the velocity below
 507 the MTZ results in the absence of mantle arrivals [Christeson et al. 2020]. Therefore, the absence of
 508 Pn arrivals could be interpreted as a decrease in velocity with depth below the Moho in the mantle.



510

511 **Figure 10: Relationship between the MTZ thickness and the critical distance:** Red dots are observed
 512 data points and blue line is a linear fit along with the equation of the linear fit (in blue text). The equation for
 513 linear trend of critical distance (y_1 in km) with respect to the thickness of the MTZ (x in m) is also shown
 514 here.

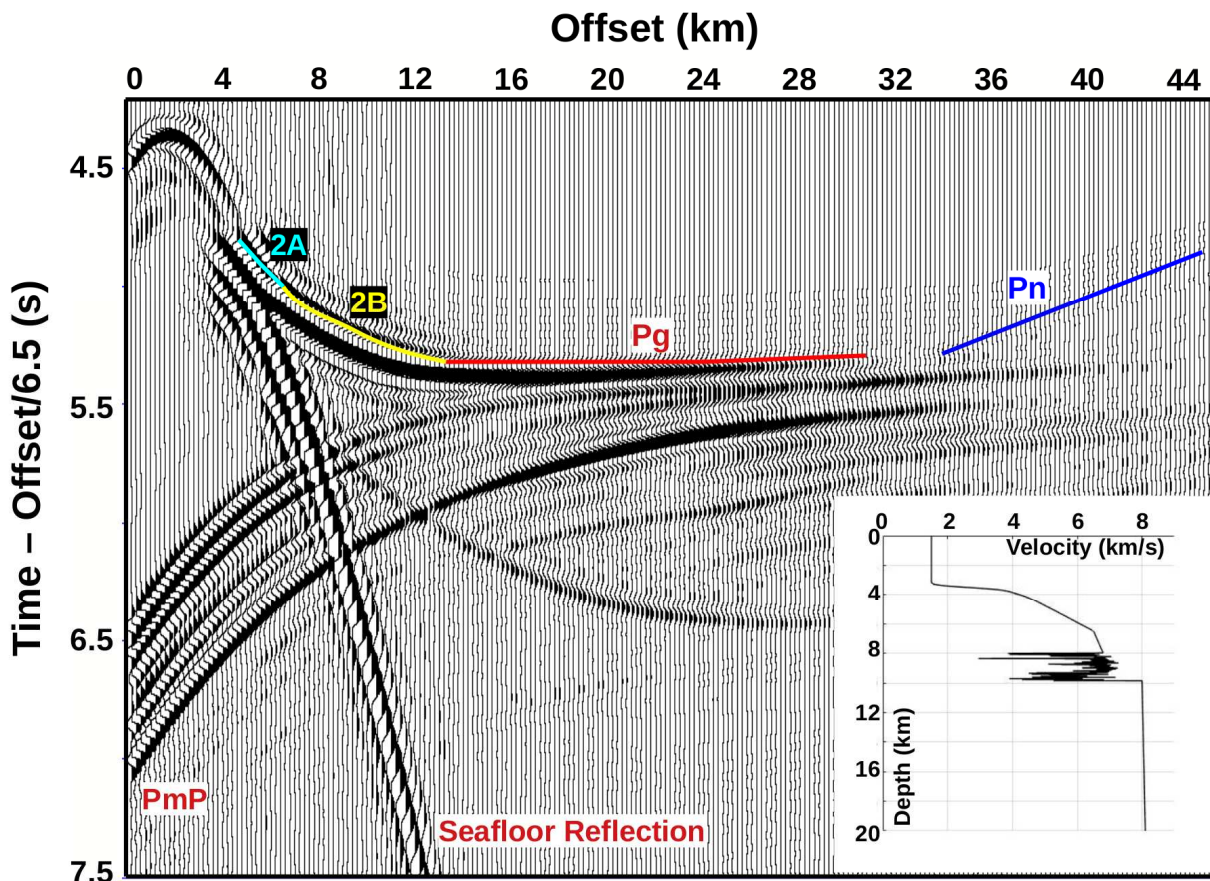
515

516 4.4 Synthetic Seismogram for Lithology from the Oman Drilling Project

517 We have used the velocity data of the ophiolite samples obtained from the recently drilled
 518 borehole in Oman for computing synthetic seismograms. There are 5 borehole sequences; GT1,
 519 GT2, GT3, CM1 and CM2, each with ~400 m thickness (Section S.2 and Figure S3 in
 520 supplementary material; [Okazaki et al. 2018; Kelemen et al. 2020]). The physical properties like P-
 521 wave velocity, bulk-density and porosity were measured for each sample from the lithology of the
 522 borehole sequence. For the synthetic seismogram modelling, we assigned GT1, GT2 and GT3
 523 sequences for the lower crust and CM1, CM2 sequences for the crust to mantle transition zone. The
 524 P-wave velocities in the X, Y and Z directions are averaged to get single P-wave velocity for each
 525 sample from the borehole. After averaging the P-wave velocity, we have extracted the samples at
 526 each 10 m interval from the borehole sequence and used their velocities to construct the 1D velocity
 527 profile of the lower crust and MTZ. The 10 m interval was decided based on the grid spacing of
 528 velocity models in all the previous cases of the lower crust and MTZ. The velocities of the upper
 529 crust and beneath the MTZ are the same as those of the synthetic models shown in Figure 3a. The
 530 presence of low velocity could have occurred due to: 1) hydrothermal circulation near the

531 spreading-ridge axis, 2) during the obduction onto the Arabian continental margin, 3) present-day
 532 weathering. The extended and the entire 1D profiles of P-wave velocity, density and porosity along
 533 with the lithology of all the borehole samples are shown in Figure S3. Although the average P-wave
 534 velocity in the lower crust increases from 6 km/s to 7 km/s, there are many low velocity layers
 535 which could be attributed to alteration. On the other hand, the average velocity in the mantle is ~5.7
 536 km/s due to serpentinization. In the original study by Okazaki et al. [2018], the samples were
 537 obtained at random depth intervals, but here we selected the sample at each 10 m interval to
 538 construct the 1D profile of the velocity model (inset of Figure 11) for synthetic seismogram
 539 modelling. We have assumed that the Moho is sharp and included the drilling results in the lower
 540 crust above the Moho. This model could be considered as a velocity model of a core complex where
 541 high velocity gabbroic rocks have been emplaced above serpentinized peridotite [Canales et al.
 542 2008; Davy et al. 2020].

543



544

545 **Figure 11: Synthetic seismograms for the Oman Model:** Whole offset (0-45 km) synthetic seismogram
 546 for the given 1D Velocity model at 10 m grid spacing (as shown in the bottom inset), which was obtained
 547 from the Oman borehole lithology [Kelemen et al. 2020]. The detailed lithology and velocity are shown in
 548 Figure S3 [Kelemen et al. 2020]. In the seismogram, a sharp Moho is included at the base of the Oman
 549 velocity model at 10 km depth. Complex reflections and interference at both near offset and far offset are
 550 observed.

551

552 The synthetic seismograms corresponding to this velocity model are more complex as
553 compared with seismograms for 1D lower crust and MTZ models (Figure 11). We observed
554 reflection from the seafloor, Pg and a strong amplitude PmP reflection. Due to the presence of
555 positive and negative velocity fluctuations in the lower crust over the background velocity of 6.5
556 km/s, we observe few strong amplitude reflections above the PmP arrival starting from zero offset.
557 Some of the multi-phase reflections merge at 26 km offset and continue as single-phase reflection
558 up to 44 km offset. Other reflections merge either with the Pg or with the PmP arrivals. The Pg and
559 PmP arrivals are not observed after 30, and 40 km offsets, respectively. The PmP is not observed
560 over the entire offset because of large dissipation of seismic energy due to velocity fluctuations in
561 the lower crust and MTZ. The seismic arrivals below and parallel to the PmP reflection are interbed
562 multiples due to the velocity structure in the lower crust. Here the Pn refraction is very weak due to
563 strong and complex reflectivity responses from the lower crust. Also, the Pg and Pn do not become
564 tangent to the PmP at far offsets due to velocity variations in the lower crust, especially due to the
565 presence of low velocities (less than 6.5 km/s).

566

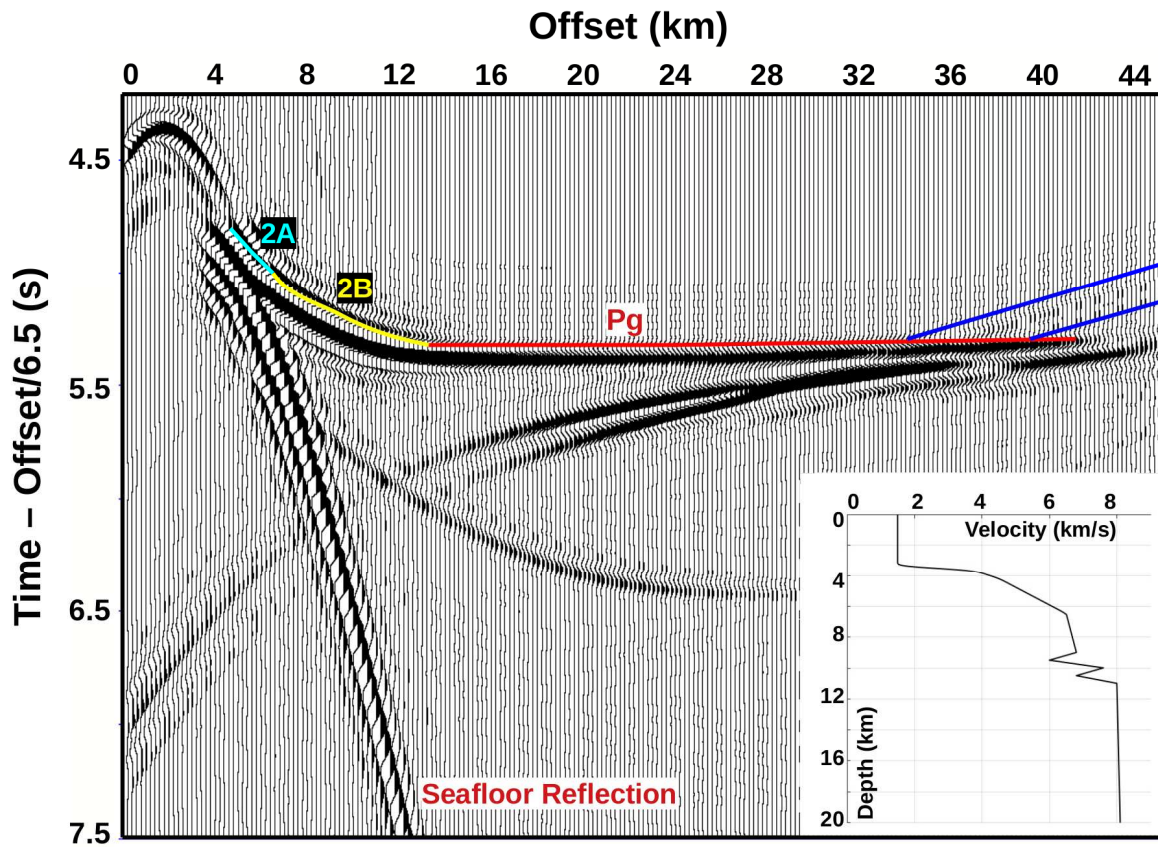
567 **4.5 Synthetic Seismogram for the Bay of Islands Ophiolites**

568 We have also analysed the synthetic seismogram for the velocity model from the Bay of
569 Islands ophiolites [Karson et al. 1984]. In this model (inset of Figure 12), the velocity linearly
570 decreases from 6.8 km/s to 6.0 km/s in the lower crust from 9 km to 9.5 km depth, then linearly
571 increases up to 7.6 km/s at 10 km depth, then decreases from 7.6 km/s to 6.8 km/s at 10.5 km depth,
572 and increases to 8 km/s at 11 km depth [Karson et al. 1984]. So this model represents layers of
573 alternate gradients of velocity like a negative (decreasing velocity) and positive (increasing
574 velocity) gradients over a 2 km thick MTZ. Karson et al. [1984] and Collins et al. [1986] have
575 carried out near offset reflection modelling, and here we extend these studies from zero to 45 km
576 offsets.

577

578 The whole offset (0-45 km) synthetic seismogram is shown in Figure 12. Two low
579 frequency reflections start at 7 s and 7.3 s at zero offset, which correspond to the two layers. With
580 the increase of the offset, the two reflections merge at 27 km offset and continue as a single phase
581 reflection till 36 km offset. The amplitude of this single phase reflection decreases between 36-38
582 km offset due to the interference effect. There is another reflection arrival starting at 26 km offset
583 below the second reflection, which merges with the single phase reflection at 38 km offset and
584 continues till 45 km. Here we observed multiphase Pn refraction; first, starting at 36 km and the
585 second at 40 km offset because of the presence of gradient velocity layers in the MTZ. A complex
586 interference between the Pg and MTZ arrivals gives the appearance that the Pg arrival continues up
587 to 42 km offset. So, when there is a cluster of gradient velocity layers in the MTZ, we observe

588 multiple wide-angle reflections depending on the number of velocity layers which eventually
 589 converge to single phase reflection at far offsets. Also, the presence of velocity layers changes the
 590 waveform of the Pn arrivals.



591
 592 **Figure 12: Synthetic seismograms for the Bay of Islands Model:** Whole offset (0-45 km) synthetic
 593 seismogram for the given 1D Velocity model of the Bay of Islands Ophiolites [Karson et al. 1984], as shown
 594 in the bottom inset. In the seismogram, the low frequency reflections at near offsets become strong two
 595 reflections at intermediate offsets (15 -26 km), merging into one PmP arrivals up to 36 km offset. The Pn
 596 arrival is a double-phase response; one starting at 36 km offset and the other at 40 km.

597
 598 **4.6 Synthetic Seismogram for a 2D Velocity model**

599 We have also created a 2D velocity model inspired from the Bay of Islands ophiolites
 600 [Collins et al. 1986]. The model has a depth of 20 km and extends over 60 km (Figure 13a). The
 601 water depth (3.5 km) and the crustal thickness (6 km) are the same as for the 1D velocity models.
 602 The MTZ is around 3 km thick (between 9.5 and 12.5 km) and has three main interfaces with
 603 heterogeneity between the top and bottom interfaces. These three interfaces are composed of the
 604 gabbro P-wave velocity of 6.7 km/s, wehrlite velocity of 7.9 km/s, harzburgite velocity of 8.1 km/s
 605 and dunite velocity of 8.2 km/s and then the mantle. In the MTZ, the gabbro heterogeneities are
 606 present in the harzburgite and wehrlite layers, as well as harzburgite and dunite heterogeneities in
 607 the gabbro and wehrlite layers. Gabbro and harzburgite sills are present in the centre of the model.
 608 Some dunite sills are present just below the MTZ top interface and gabbro sills are just above the

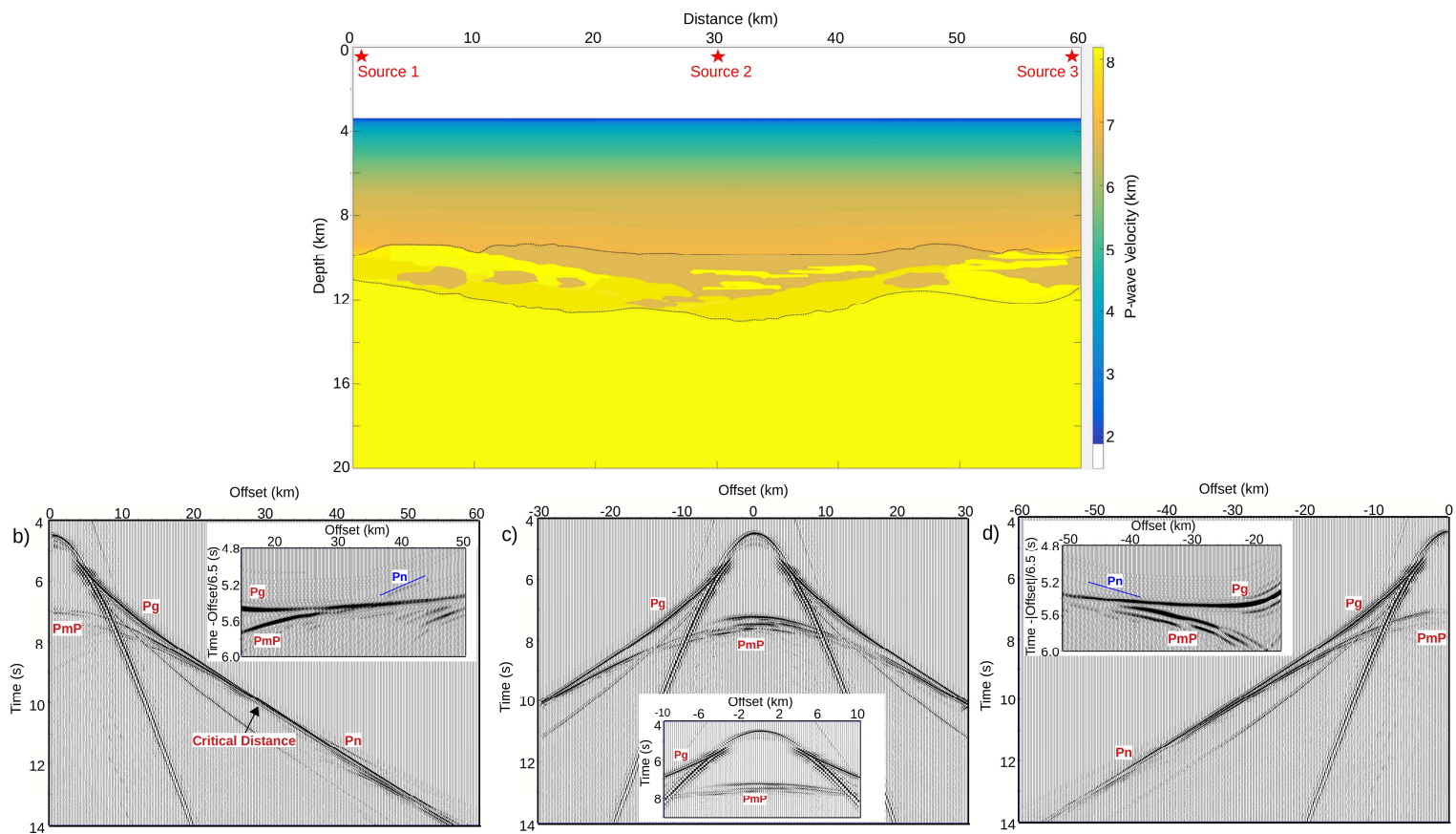
609 MTZ bottom interface. We computed synthetic seismograms for this model using three source
610 positions, one at either end of the model at 0 and 60 km and one in the centre of the model at 30 km.
611

612 We computed a 0-60 km ultra-long offset synthetic seismogram (Figure 13b) for the source
613 at the left end of the model (source 1). We observed Pg and seafloor reflection. Between 0 and 10
614 km offset, we observed low-amplitude and multiphase (shingled) PmP reflections. Due to
615 interference and merging of multiphase reflections, the amplitude of the PmP begins to increase
616 after 12 km, and becomes maximum at the critical distance of 28 km in this case. The PmP is found
617 as a continuous and single phase reflection between 28 and 38 km offsets. The PmP reflection
618 becomes discontinuous and multiphase after 38 km offset, with a substantially higher amplitude
619 than near offset reflection (0-10 km). The amplitude of the Pg arrival weakens after 24 km offset
620 and it becomes tangent to the PmP at 28 km offset near the critical distance (inset of Figure 13b),
621 while the Pn is not tangent to the PmP at the critical distance. The Pn has a low amplitude which
622 begins at 36 km and lasts until 44 km. Due to the MTZ strong and complex reflectivity response,
623 the amplitude of the Pn refraction arrival is very weak. The presence of the MTZ interfaces and the
624 small-scale heterogeneities within the MTZ result in complex and multiphase PmP reflections at
625 near offset (low amplitude) and far offset (high amplitude), as well as weakening of the Pg
626 amplitude just before the critical distance and weak-amplitude of the Pn after the critical distance.

627
628 We computed synthetic seismograms for the source at the centre of the model (source 2 at
629 30 km) for a 30 km offset in both directions (Figure 13c). The PmP reflection is multiphase and
630 discontinuous again between -10 and 10 km offsets. Some of them have a higher amplitude and are
631 separated by reflections with a lower amplitude. When compared to reflections from 0 to -10 km
632 offset, the amplitude of the reflections from 0 to 10 km offset is considerably higher. The amplitude
633 of these reflections decreases until they are -14 km (on the left side) and 17 km (on the right side)
634 from the source. Due to the interference and merging of multiphase reflections with increasing
635 offsets, the amplitude begins to increase beyond -14 km and 17 km offsets on both sides. In
636 comparison to the right side of the model, the PmP reflection is more continuous (and
637 homogeneous) on the left side. Because of the heterogeneous structure of the MTZ, the PmP
638 reflection is again complex and multiphase (and discontinuous).

639
640 Finally, we computed 60-km ultra-long synthetic seismograms (Figure 13d) for the source at
641 60 km distance (source 3). In this case, the PmP reflection is more complicated than that in Figure
642 13b. Between 0 and -5 km, it has a very low amplitude. The PmP reflection is observed as
643 multiphase (discontinuous) starting at -10 km offset and continue until the end of the model. Its
644 amplitude begins to increase between -10 and -40 km offsets due to the interference of multiphase

645 reflections (inset of Figure 13d). After -40 km offset, its amplitude starts decreasing. At a very far
 646 offset (-38 km), the Pg becomes tangent to the multiphase PmP reflection. Due to the presence of
 647 gabbro heterogeneities (low velocity) in the MTZ, the Pn has a very weak amplitude between -38
 648 and -47 km, and is not tangent to PmP. Due to the MTZ strong and complex reflectivity response,
 649 the Pn refraction shows a very weak amplitude. When compared to the Pn and the PmP observed in
 650 Figure 13b, here, the Pn has a lower amplitude and the PmP has a higher amplitude. Between 28
 651 and 38 km offsets, the PmP is observed as single phase when the source is at the left end of the
 652 model (Figure 13b) and as multiphase (discontinuous) when the source is at the right end of the
 653 model for the same offset range (Figure 13d). The heterogeneous structure of the MTZ is
 654 responsible for the differences in the nature of the PmP reflections at far offsets.
 655



657 **Figure 13: Modelling of a 2D velocity profile:** a) 2D velocity model for the Bay of Islands ophiolites
 658 recreated from Collins et al. [1986]. The top and bottom interfaces of the heterogeneous MTZ layer are
 659 marked by the dashed lines and consist of layers and heterogeneities of gabbro (velocity = 6.7 km/s),
 660 wehrlite (7.9 km/s), harzburgite (8.1 km/s), dunite (8.2 km/s). Red stars show the position of three sources
 661 for computing the synthetic seismogram. b) Ultra-long 0-60 km offset synthetic seismogram for a 2D
 662 velocity model when source 1 is at the left end of the model. Inset shows the waveforms of the Pg, Pn and
 663 PmP arrivals between 15-50 km at the reduction velocity of 6.5 km/s. c) 60 km long (-30 to 30 km) synthetic
 664 seismogram for source 2 at the centre of the model. Inset shows the detailed waveform of the PmP
 665 reflections between -10 and 10 km. d) Ultra-long 0-60 km offset seismogram for source 3 at the right end of

666 the model. Inset shows the waveforms of the Pg, Pn and PmP between -15 and -50 km offset at a reduction
667 velocity of 6.5 km/s.

668

669 In a nutshell, near offset PmP shows strong amplitude reflection when the MTZ is uniform
670 and sharp (as observed in 1D models). The waveforms of the PmP and the Pn, however, are affected
671 by the MTZ complex velocity structure. The near offset PmP amplitude is quite low, but it increases
672 as the offset increases. The presence of high and low velocity heterogeneities in the MTZ causes the
673 PmP reflection to be discontinuous (multiphase) and the Pn amplitude to be very weak. Because of
674 the heterogeneous structure of the MTZ, the interference and merging of multiphase PmP reflection
675 depend on the source-receiver geometry.

676

677 **5 Discussion**

678 **5.1 Lower crustal velocities**

679 In normal oceanic crustal settings, ray-based travel time tomography of Pg arrivals only
680 samples down to the upper crust-lower crust boundary e.g., [White et al. 1992; Christeson et al.
681 2010; Christeson et al. 2019; Vaddineni et al. 2021] as Pg and PmP arrivals interfere with each
682 other and have more or less the same travel times in the case of a positive velocity gradient in the
683 lower crust (e.g. Figure 6). Therefore, the velocity in the lower crust is mainly estimated using the
684 arrival times of PmP arrivals, and hence there is a trade-off between the Moho depth and the lower
685 crustal velocity estimation [Jarchow and Thompson, 1989; White et al. 1992; Joussetin et al. 2012;
686 Christeson et al. 2019; Vaddineni et al. 2021]. If there is a positive velocity gradient in the lower
687 crust, the rays must turn in the lower crust, and hence the waveform of the combined Pg and PmP
688 arrivals should contain information about the lower crust. Using appropriate waveform inversion
689 strategy, such as elastic waveform inversion [e.g. Shipp and Singh, 2002], one should be able to
690 retrieve information about the velocity gradient in the lower crust.

691

692 Shadow zones are generally observed near the ridge axis, indicating the presence of low
693 velocity in the lower crust possibly associated with the presence of partial melt in the lower crust
694 [Toomey et al. 1990; Jian et al. 2017]. Low velocity in the lower crust has been observed using
695 expanding spread profile over the 118 Ma slow spreading Atlantic crust [Mithal and Mutter, 1989],
696 otherwise they are rarely observed over the normal oceanic crust. On the other hand, most of the
697 tomographic inversion results indicate that the velocity increases in the lower crust, say from 6.5
698 km/s to 7 km/s [Korenaga et al. 2000; Van Avendonk et al. 2001; Holmes et al. 2008; Planert et al.
699 2009; Christeson et al. 2010], which means Pg arrivals would have a large amplitude at far offsets,
700 but it would interfere with the PmP arrivals. However, the triplication is likely to be absent due to
701 the presence of a high velocity gradient in the lower crust. Therefore, the lateral extent of the

702 triplication could be used to characterise the velocity gradient in the lower crust, i.e. a wide
703 triplication may indicate zero or very low velocity gradient in the lower crust whereas the absence
704 of triplication would suggest a higher velocity gradient in the lower crust. The OBS data shown in
705 Figure 1 do not have any triplications, suggesting the presence of a positive velocity gradient in the
706 lower crust, consistent with the tomographic results [Vaddineni et al. 2021].

707

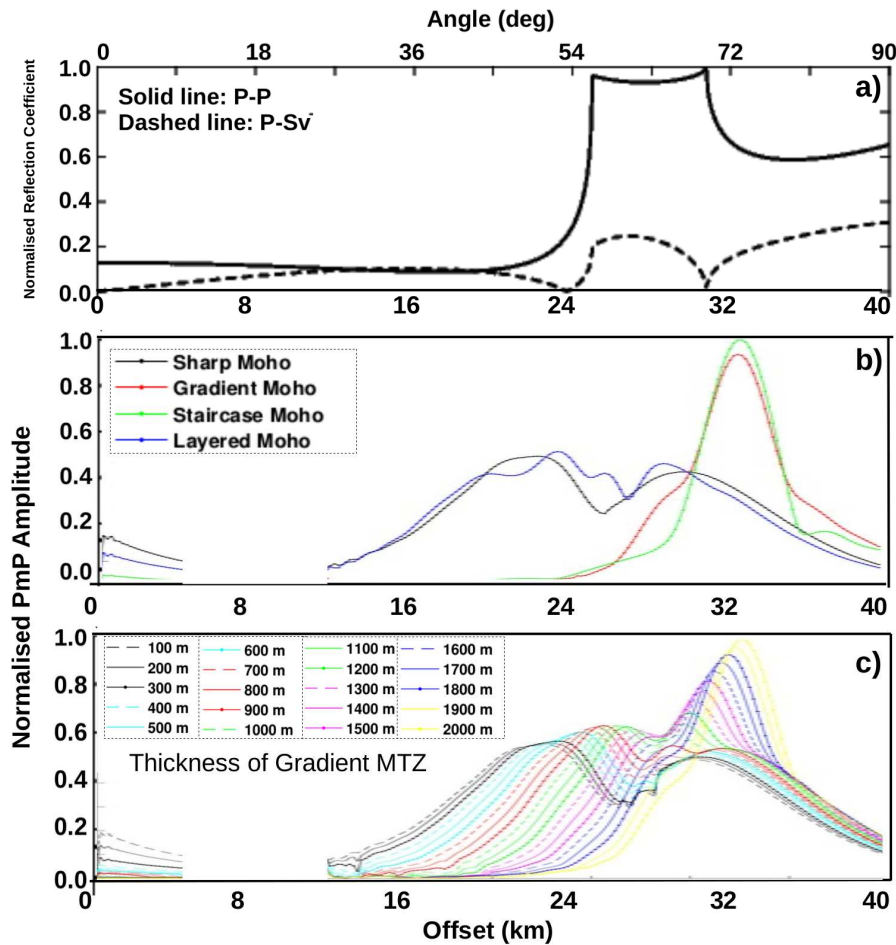
708 Waveforms of Pg arrivals are influenced by the structures in the lower crust (Figure 5),
709 especially by the layering in the lower crust (Figure 5c). Although the high-frequency Pg rays do
710 not travel through the lower crust, the low frequency wavefields do sample the lower crust. Guo et
711 al. [2021a] have recently performed full waveform inversion of Pg arrivals using OBS data from the
712 Atlantic Ocean and discovered the presence of layering in the lower crust. They also show that
713 layered structures, similar to Figure 3e, instead of gradational layering (Figure 3d), are required to
714 explain their observation, which is consistent with our analyses (Figure 5c). Therefore, we
715 recommend that waveform and amplitude based analyses should be performed to extract
716 information about the lower oceanic crust.

717

718 **5.2 Amplitude Variation with Offset (AVO) analysis of MTZ reflections**

719 Our synthetic seismogram modelling of the MTZ indicates that the amplitude versus offset
720 behaviour of the PmP arrivals are different for different velocity structures of the MTZ. Hence, we
721 performed an AVO analysis for those models in terms of reflection coefficient (RC) [Chapman,
722 1994; Thomson et al. 1986]. The amplitude (or energy) of the reflected and transmitted waves vary
723 with the angle of incidence. As the angle of incidence approaches the critical value, the transmitted
724 P-wave energy goes to zero, and most of the energy is reflected as P-wave. We first computed the
725 synthetic AVO response for a two-layer model assuming layer 1 as a lower crust with $V_{p1} = 6.5$
726 km/s , $V_{s1} = 3.705 \text{ km/s}$, $\rho_1 = 2.778 \text{ kg/m}^3$, and layer 2 as a sharp MTZ with $V_{p2} = 8.0 \text{ km/s}$, $V_{s2} =$
727 4.560 km/s , $\rho_2 = 2.926 \text{ kg/m}^3$. The normalised RC for such two-layer configuration using a layered-
728 matrix approach [Aki and Richard, 1978] is shown in Figure 14a. Here, we have converted the
729 angle (in degrees) to approximate offset (in km) assuming the Moho interface at 9.5 km depth. The
730 RC for the P-to-P and P-to-Sv (P-wave converted to the vertically polarised S-wave) reflections
731 from the Moho are shown in Figure 14a, where P-P RC is 0.12 at zero offset and gradually
732 decreases with offset up to 20 km and then increases suddenly to a peak value of 1.0 near the
733 critical angle ($\sim 54^\circ$) at an approximate distance of 24 km. The RC for P-P remains high in the post-
734 critical regime, but two peaks are observed, one associated with the P-wave critical angle and the
735 other with the S-wave critical angle. The RC for the converted S-wave is zero at zero offset then
736 slowly increases and becomes maximum at $\sim 16 \text{ km}$ before decreasing to zero at the critical offset,
737 and then again increases beyond 24 km offset. Note the inverse correlation between the P-P and P-

738 Sv reflection coefficients. These results indicate that RC for P-Sv is of similar scale as that for the
 739 P-P at offset >8 km and hence should be taken into account for any quantitative analyses of the
 740 MTZ.



741
 742 **Figure 14: Amplitude versus offset (AVO) for MTZ models:** a) Normalised reflection coefficient (RC) as
 743 a function of angle (offset) for a simple two layer model containing lower crust and upper mantle with the
 744 Moho as an interface. The incident angle is converted to approximate offset assuming the Moho interface at
 745 9.5 km and the crustal velocity of 6 km/s. b) Normalised PmP AVO for the four different models for MTZ as
 746 shown in Figure 3: sharp (black line), gradient (red line), staircase (green line) and layered (blue line). c)
 747 Normalised PmP AVO for different thicknesses of gradient MTZ starting from 100 m to 2000 m. The gap
 748 between 7 and 14 km is due to interference with seafloor reflection.

749
 750 To extend the above analysis to a realistic case, we compared the reflection amplitude for
 751 various MTZ models in which the amplitudes corresponding to the PmP reflections are extracted
 752 from synthetic seismograms for the different models discussed above. First, the normalised PmP
 753 AVO for the four MTZ models (sharp Moho, gradient Moho, staircase Moho, layered Moho) are
 754 shown in Figure 14b. For the sharp and layered MTZ, the amplitude decreases up to 5 km offset.
 755 We do not show the amplitudes of the PmP arrivals between 7 and 14 km offsets because of the
 756 interference of the PmP arrivals with the seafloor reflection and the Pg multiple arrivals. Beyond 14
 757 km offset, the amplitude for the sharp and the layered Moho rapidly increases, attain the first peak

758 value near the critical distance at ~23 km offset and the second peak at ~30 km offset. Between 23-
759 30 km offset, the amplitude corresponding to the layered MTZ shows a complex behaviour due to
760 the layering of the velocity below the sharp MTZ. Compared to these two models, the amplitude of
761 the PmP arrival for the staircase Moho is low from zero up to 24 km offset due to the absence of
762 strong PmP reflection, and it suddenly starts increasing after 24 km offset, with a very large narrow
763 peak at 33 km offset (critical distance) where a strong amplitude Pn arrival is tangent to PmP arrival
764 (Figure 8b). On the other hand, for the gradient MTZ, the PmP amplitude is zero at zero offset and
765 starts increasing after 22 km offset as observed in the synthetic seismograms (Figure 8a), with a
766 peak at 33 km but over a slightly wider offset range as compared to the staircase MTZ.

767

768 We observed two peaks for the PmP reflection amplitudes for the sharp and layered MTZ, as
769 indicated by the simple two-layer model (Figure 14a), but only one peak for the gradient MTZ and
770 staircase models in a narrow offset range around 33 km. To understand the transition from one
771 peak to two peaks, we extracted the PmP amplitudes for different gradient MTZ models where the
772 MTZ thickness increased from 300 m to 2000 m at 100 m interval. The corresponding AVO
773 response is shown in Figure 14c. As expected, the lower the thickness of the gradient MTZ is the
774 higher the amplitude of the PmP reflection is at near offsets (0-5 km). When the thickness of the
775 MTZ is more than 1100 m, the PmP amplitude is zero at the zero offset. After 14 km offset, the
776 PmP amplitude gradually increases with increasing offset. When the thickness of the MTZ is less
777 than 1400 m, we observed two peaks in the AVO response: first in the offset range of 22-27 km and
778 the second in the 31-33 km range. Furthermore, the critical distance increases with increasing
779 thickness of the MTZ. The PmP AVO for models with a thickness greater than 1400 m shows only
780 one peak in the offset range of 30-34 km along with the increase in the critical distance with
781 increasing offset. So the transition from two broad high amplitude peaks to a single narrow peak in
782 the AVO response depends on the thickness of the MTZ. Our results indicate that when the
783 thickness of the MTZ is less than ~1.75 times of dominant seismic wavelength (which is 800 m in
784 our case because the dominant frequency of the source is 10 Hz and the P-wave velocity at the
785 Moho is 8000 m/s), there are two high amplitude peaks for the PmP reflection in AVO response.
786 Also note that the AVO response shown in Figure 14a is based on single-layer-matrix calculation
787 whereas the normalised PmP amplitudes are extracted from synthetic seismograms which are
788 obtained from the finite difference solution and hence we were able to capture the frequency
789 dependent (MTZ thickness or structure) nature of PmP reflections. These results confirm the above
790 analyses demonstrating that the PmP arrivals for a thick MTZ (gradient or staircase) lie in a narrow
791 offset range around the critical distance. It should be noted that the location of the offset range
792 around critical distance will depend on the crustal thickness and the velocity in the crust. The

793 presence of a broad high amplitude PmP arrival in the real data shown in Figure 1 indicates that the
794 Moho is likely to be a sharp boundary [Vaddineni et al. 2021].

795

796 The above analyses indicate that some insight could be obtained about the MTZ from the
797 AVO analyses from high-quality zero offset to 40-45 km offset data. However, in real world, we
798 either have Moho reflections at near offsets from MCS data or wide-angle PmP arrivals from ocean
799 bottom seismometer data (OBS) over 15-40 km offset range with the interference of the Pg and Pn
800 arrivals around the critical distance (Figure 1). Since the offset range in the MCS is short and the
801 signal-to-noise ratio for OBS data is generally low, especially when the seafloor morphology is
802 rough, the AVO analysis for MTZ has never been performed.

803

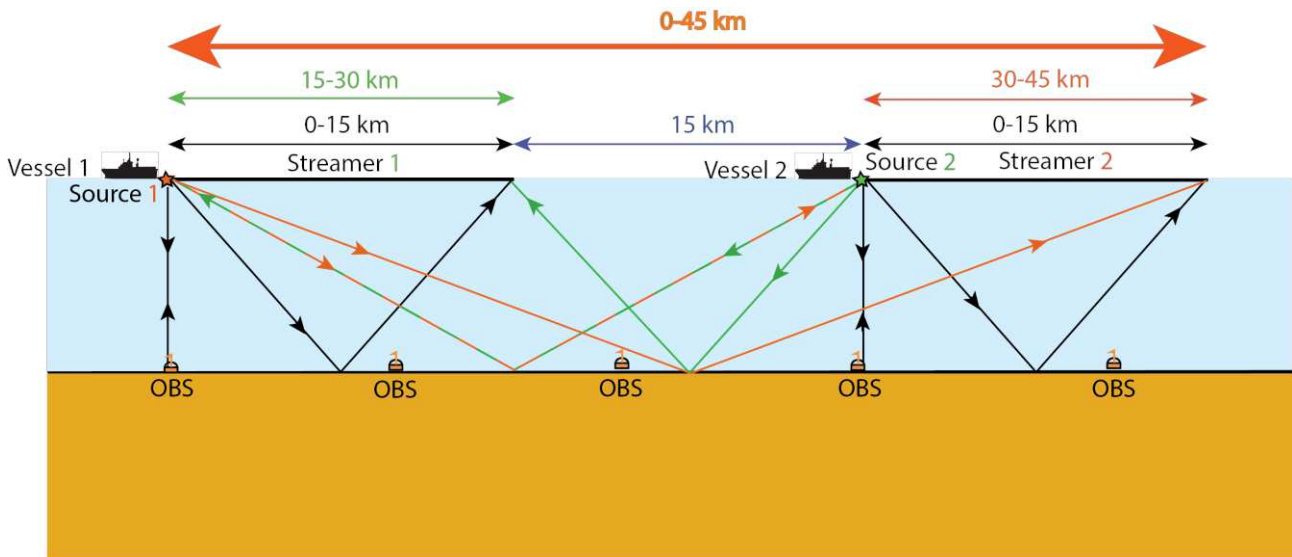
804 **5.3 Limits of the present study and suggestions for the future:**

805 We have mainly focused on 1D structures in the lower crust and MTZ for certain crustal
806 velocity structures and upper mantles, with one case of 2D model, based on the Bay of Islands
807 ophiolites. Our findings will change depending upon the change in these parameters. Furthermore,
808 the Earth is 3D visco-elastic anisotropic, and one has to take all these effects into account in
809 quantifying the nature of the MTZ. The presence of 3D structures would create more complex
810 waveforms and amplitude versus offset variations, whereas the attenuation due to visco-elasticity
811 will cause a decrease in amplitude with offset, and may even change the waveforms.

812

813 Secondly, most of near offset data are acquired using 3-6 km long streamers and wide-angle
814 data using OBSs sparsely deployed on the seafloor where the signal-to-noise ratio is generally very
815 poor, and hence these data are not suitable for the type of analyses suggested here. In order to
816 provide a quantitative information about the lower crust and MTZ, one would require high-quality
817 multi-channel type data recorded from 0 to 40-50 km, with a shot interval of 100-200 m. To obtain
818 such an offset, we suggest to acquire two-vessel data, with each vessel carrying 15-km long
819 streamers and identical sources, spaced at 30 km, moving in the same direction and shooting
820 alternatively (Figure 15). When Vessel 1 shoots, these shots will be recorded on Streamer 1,
821 providing offsets of 0-15 km (black arrows), which will also be recorded by Streamer 2, with offsets
822 from 30 to 45 km (orange arrows). When Vessel 2 shoots, the data will be recorded by Streamer 1
823 recording an offset range of 15 to 30 km (green arrows), and also by Streamer 2 recording a
824 duplicate of the 0-15 km offset range. Each vessel will shoot at 100 m interval in an alternate mode.
825 As data recording will be continuous, the two vessels data could be arranged in such a way that a
826 continuous offset range from 0 to 45 km can be achieved at 100 m shot interval.

827



828

829 **Figure 15: Ultra-long offset seismic reflection data acquisition design:** 0-45 km long offset novel two-
 830 ship survey design with ray diagrams, each vessel carrying a large source and a 15 km long streamer. Each
 831 vessel carries 15-km long streamers and identical sources, spaced at 30 km, moving in the same direction and
 832 shooting alternatively. Shots from Vessel 1 recorded on Streamer 1 will provide 0-15 km offset MCS data
 833 (black arrows), and shots recorded by Streamer 2 will provide 30 to 45 km offset data (orange arrows).
 834 Shots from Vessel 2 recorded by Streamer 1 will provide 15 to 30 km offset data (green arrows). OBSs are
 835 placed on the seafloor.

836

837 Mithal and Mutter [1989] have shown using expanding spread profile, where MCS
 838 technology was used, one could record Moho reflections continuously starting from zero offset to
 839 post-critical distance. Guo et al. [2021a] have recently demonstrated that the full elastic waveform
 840 inversion of Pg arrivals could retrieve information about the lower crustal layer. Neves and Singh
 841 [1996] have indicated that full waveform inversion of continuous MCS seismic data from zero
 842 offset to critical angle could provide complete information about the sub-surface with a resolution
 843 of the quarter of the wavelength. Therefore, 2D elastic full waveform inversion of 0-45 km MCS
 844 type data should provide complete information about the lower crust, the MTZ and the structure of
 845 the upper mantle. One should note that wide-angle reflection amplitude from the lower crust and the
 846 MTZ do not simply depend on the P-wave velocity but also depends on the S-wave velocity, and
 847 therefore, elastic, not acoustic, waveform inversion should be used to characterise the lower crust
 848 and the MTZ.

849

850 Figure 14 indicates that the reflection coefficient suddenly increases from ~ 0.10 at 20 km
 851 offset to ~ 1.0 at 24 km offset, and shows a complex behaviour between 24 and 32 km offset, which
 852 may pose some problems in applying conventional waveform inversion [Shipp and Singh, 2002].
 853 In this case a global search algorithm should be used. Guo et al. [2021b] have applied a global
 854 search algorithm based a Bayesian Monte Carlo approach to a limited offset OBS data, and showed

855 that the MTZ could be equally explained by a sharp and a layered MTZ. However, by having a
856 good starting velocity model based on 0-45 offset continuous PmP arrivals, this non-linearity in
857 waveform inversion could be mitigated.

858

859 **6 Conclusions**

860 The waveform and interaction of Pg (crustal refractions), PmP (reflection from the Moho)
861 and Pn (upper mantle refraction) are studied by analysing synthetic seismograms for a suite of 1D
862 velocity models of the lower crust and the MTZ and a 2D model inspired from the Bay of Islands
863 ophiolites. The following conclusions can be drawn from our modelling studies:

864

865 1. The wide-angle seismic reflection response of the MTZ does not only depend on the velocity
866 structure of the MTZ but also on the velocity structure in the lower crust.

867

868 2. The size and the lateral extent of the triplication involving Pn, Pg and PmP arrivals depend on
869 velocity gradient in the lower crust and the nature of the MTZ.

870

871 3. The amplitude of near-offset Moho reflection decreases as the thickness of the gradient MTZ
872 increases, and becomes zero when the thickness is greater than 1100 m.

873

874 4. The amplitude variation with an offset (AVO) analysis of MTZ models suggests that the critical
875 distance increases linearly with the increase in the thickness of the MTZ.

876

877 5. When the thickness of the MTZ is less than ~1.75 times the dominant seismic wavelength, two
878 high-amplitude peaks for PmP reflections occur at critical distances associated with P- and S-wave
879 velocities.

880

881 6. For a thicker MTZ only one large peak at large offset is observed, suggesting that AVO analyses
882 could provide information about the MTZ.

883

884 Our study indicates that a continuous recording of 0-45 km offset data using MCS technology with
885 a source spacing of 100-150 m combined with elastic full-waveform inversion should provide a
886 complete information about the elastic properties of the lower crust, MTZ and upper mantle. These
887 results combined with an effective medium theory analysis [Taylor and Singh, 2002] and rock and
888 mineral properties [Hacker and Abers, 2004] would allow to predict lithology, which in turn would
889 help to shed light upon the physical and chemical processes responsible for the formation and
890 evolution of the oceanic crust and upper mantle.

891

892 **Credit authorship contribution statement**

893 VI performed the modelling and wrote the paper. SCS designed the project, supervised the project
894 and wrote the paper.

895

896 **Declaration of Competing Interest**

897 We state that this manuscript contains original modelling results, ideas and/or interpretations not
898 previously published or under consideration for publication elsewhere (including electronic media
899 and databases).

900

901 **Acknowledgements**

902 This project was funded by the European Research Council Advanced Grant agreement No. 339442
903 TransAtlanticILAB. Venkata Vaddineni provided OBS data shown in Figure 1. We are thankful to
904 Natsue Abe and Keishi Okazaki for providing the lithology and velocity logs shown in Figure S3.
905 Constructive comments from two anonymous reviewers have helped to improve the manuscript
906 significantly. This is the Institut de Physique du Globe publication number X. This paper is
907 dedicated to Professor Adolph Nicolas who provided valuable insight about the magma chamber,
908 lower crust and MTZ during memorable field trips. One of us (SS) would like to thank Françoise
909 Boudier and David Joussetin for leading the field trip to Oman in January 2020, that allowed to
910 prepare the composite figure shown in Figure 2.

911

912 **Data Availability**

913 The study is based on synthetic models and data. Synthetic data will be uploaded in SEG-Y format
914 prior to publication. Data shown in Figure 1 are archived at Pangea:
915 (<https://doi.pangaea.de/10.1594/PANGAEA.914912>) and will be made available upon request. Data
916 shown in Figure S3 are available through the IODP Website.

917

918 **References**

919 Aghaei, O., Nedimović, M. R., Carton, H., Carbotte, S. M., Canales, J. P., Mutter, J. C., 2014.
920 Crustal thickness and Moho character of the fast spreading East Pacific Rise from 9° 42' N to 9° 57'
921 N from post-stack migrated 3D MCS data. *Geochem. Geophys. Geosyst.* 15(3), 634-657.

922

923 Aki, K., and Richards, P. G., 1978, *Quantitative seismology: Theory and methods*, vol. I: W. H.
924 Freeman.

925

926 Arnulf, A. F., Singh, S. C., Pye, J. W., 2014. Seismic evidence of a complex multi-lens melt
927 reservoir beneath the 9°N Overlapping Spreading Center at the East Pacific Rise, *Geophys. Res.*
928 *Lett.* 41, 6109-6115.

929

930 Audhkhasi, P., Singh, S. C., 2019. Seismic Structure of the Upper Crust From 0–75 Ma in the
931 Equatorial Atlantic Ocean on the African Plate Using Ultralong Offset Seismic Data. *Geochem.*
932 *Geophys. Geosyst.* 20(12), 6140-6162.

933

934 Backus, G. E., 1962. Long-wave elastic anisotropy produced by horizontal layering. *J. Geophys.*
935 *Res.* 67(11), 4427–4440.

936

937 Barth, G. A., 1994. Plate boundary geometry to Moho depths within the 9 03' N and 12 54' N
938 overlapping spreading centers of the East Pacific Rise. *Earth Planet. Sci. Lett.* 128(34), 99-112.

939

940 Barth, G. A., Mutter, J. C., 1996. Variability in oceanic crustal thickness and structure:
941 Multichannel seismic reflection results from the northern East Pacific Rise. *J. Geophys. Res.*
942 101(B8), 17951-17975.

943

944 Boudier, F., Nicolas, A., 1995. Nature of the Moho transition zone in the Oman ophiolite. *J. Petrol.*
945 36(3), 777-796.

946

947 Boudier, F., Nicolas, A., Ildefonse, B., 1996. Magma chambers in the Oman ophiolite: fed from the
948 top and the bottom. *Earth Planet. Sci. Lett.* 144, 239-250.

949

950 Brocher, T. M., Karson, J. A., Collins, J. A., 1985. Seismic stratigraphy of the oceanic Moho based
951 on ophiolite models. *Geology* 13(1), 62-65.

952

953 Brocher, T. M., Frazer, L. N., 1987. A comparison of two sets of synthetic reflection seismograms
954 for a complex two dimensional model of the oceanic crust-mantle transition. *Geophys. Res. Lett.*
955 14(8), 801-803.

956

957 Canales, J. P., Tucholke, B. E., Xu, M., Collins, J. A., DuBois, D. L., 2008. Seismic evidence for
958 large-scale compositional heterogeneity of oceanic core complexes. *Geochem. Geophys. Geosyst.*
959 9(8), Q08002

960

961 Cannat, M., 1993. Emplacement of mantle rocks in the seafloor at mid-ocean ridges. *J. Geophys.*
962 *Res.* 98, 4163-4172.
963
964 Carbonell, R., Gallard, J., Perez-Estaun, A., 2002. Modelling and imaging the Moho transition: the
965 case of the southern Urals. *Geophys. J. Int.* 149, 134-148.
966
967 Carbotte, S. M., Arnulf, A., Spiegelman, M., Lee, M., Harding, A., Kent, G., Canales, J. P.,
968 Nedimovic, M., 2020. Stacked sills forming a deep melt-mush feeder conduit beneath Axial
969 Seamount. *Geology*, 48, 693-697.
970
971 Chapman, C. H., 1994. Reflection/transmission coefficient reciprocities in anisotropic media.
972 *Geophys. J. Int.* 116(2), 498-501.
973
974 Christeson, G. L., Karson, J. A., McIntosh, K. D., 2010. Mapping of seismic layer 2A/2B boundary
975 above the sheeted dike unit at intermediate-spreading crust exposed near the Blanco Transform.
976 *Geochem. Geophys. Geosyst.* 11, Q03015.
977
978 Christeson, G. L., Goff, J. A., Reece, R. S., 2019. Synthesis of Oceanic Crustal Structure From Two
979 Dimensional Seismic Profiles. *Rev. Geophys.* 57(2), 504-529.
980
981 Christeson, G. L., Reece, R. S., Kardell, D. A., Estep, J. D., Fedotova, A., Goff, J. A., 2020. South
982 Atlantic Transect: Variations in Oceanic Crustal Structure at 31°S. *Geochem. Geophys. Geosyst.*
983 21(7), e2020GC009017.
984
985 Collier, J. S., Singh, S. C., 1998. Poisson's ratio structure of young oceanic crust. *J. Geophys. Res.*
986 103(B9), 20981-20996.
987
988 Collins, J. A., Brocher, T. M., Karson, J. A., 1986. Two-dimensional seismic reflection modeling of
989 the inferred fossil oceanic crust/mantle transition in the Bay of Islands ophiolite. *J. Geophys. Res.*
990 91(B12), 12520-12538.
991
992 Cook, F. A., White, D. J., Jones, A. G., Eaton, D. W., Hall, J., Clowes, R. M., 2010. How the crust
993 meets the mantle: Lithoprobe perspectives on the Mohorovičić discontinuity and crust–mantle
994 transition. *Can. J. Earth Sci.* 47(4), 315-351.
995

996 Davy, R.J., Collier, J.S., Henstock, T., the VoiLA Consortium, 2020. Wide-angle seismic imaging
997 of two modes of crustal accretion in mature Atlantic Oceanic crust, *J. Geophys. Res.* 125,
998 Doi:10.1029/2019JB019100
999

1000 Detrick, R., Buhl, P., Vera, E., Mutter, J., Orcutt, J., Madsen, J., Brocher, T., 1987. Multi-channel
1001 seismic imaging of a crustal magma chamber along the East Pacific Rise, *Nature* 326, 35–41.
1002

1003 Dick, H. J., Sinton, J. M., 1979. Compositional layering in alpine peridotites: evidence for pressure
1004 solution creep in the mantle. *J. Geol.* 87(4), 403-416.
1005

1006 Eittreim, S. L., Gribidenko, H., Helsley, C. E., Sliter, R., Mann, D., Ragozin, N., 1994. Oceanic
1007 crustal thickness and seismic character along a central Pacific transect. *J. Geophys. Res.* 99(B2),
1008 3139-3145.
1009

1010 Ewing, M., Press, F., 1950. Crustal structure and surface-wave dispersion. *Bull. Seism. Soc. Am.*
1011 40(4), 271-280.
1012

1013 Ewing, M., Press, F., 1952. Crustal structure and surface-wave dispersion. part II Solomon Islands
1014 earthquake of July 29, 1950. *Bull. Seism. Soc. Am.* 42(4), 315-325.
1015

1016 Foulger, G. R., Du, Z., Julian, B. R., 2003. Icelandic-type crust. *Geophys. J. Int.* 155(2), 567-590.
1017

1018 Fowler, C. M. R., Keen, C. E., 1979. Oceanic crustal structure - Mid-Atlantic Ridge at 45° N.
1019 *Geophys. J. Int.* 56(1), 219-226.
1020

1021 Fuchs, K., Müller, G., 1971. Computation of synthetic seismograms with the reflectivity method
1022 and comparison with observations. *Geophys. J. Int.* 23(4), 417-433.
1023

1024 Grevemeyer, I., Weigel, W., Jennrich, C., 1998. Structure and ageing of oceanic crust at 14 S on the
1025 East Pacific Rise. *Geophys. J. Int.* 135(2), 573-584.
1026

1027 Guo, P., Singh, S. C., Vaddineni, V. A., Grevemeyer, I., Saygin, E., 2020a. In situ lower crust
1028 accretion by melt sill injection revealed by seismic layering, *Nat. Geosci.* (preprint:
1029 <https://www.researchsquare.com/article/rs-145281/v1>).
1030

1031 Guo, P., Singh, S. C., Vaddineni, V. A., Visser, G., Grevemeyer, I., Saygin, E. 2020b. Nonlinear
1032 full waveform inversion of wide-aperture OBS data for Moho structure using a trans-dimensional
1033 Bayesian method. *Geophys. J. Int.* 224(2), 1056-1078.
1034

1035 Hacker, B.R., Abers, G. A., 2004. Subduction factory 3: An Excel worksheet and macro for
1036 calculating the density, seismic wave speeds, and H₂O contents of mineral and rocks at pressure
1037 and temperature. *Geochem. Geophys. Geosyst.* 5, Q01005.
1038

1039 Harding, A. J., Orcutt, J. A., Kappus, M.E., Vera, E.E., Mutter, J. C., Buhl, P., Detrick, R. S.,
1040 Brocher, T. M., 1989. The structure of young oceanic crust at 13° N on the East Pacific Rise from
1041 expanding spread profile. *J. Geophys. Res.* 94, 12,163-12,196.
1042

1043 Helmberger, D. V., Morris, G. B., 1969. A travel time and amplitude interpretation of a marine
1044 refraction profile: primary waves. *J. Geophys. Res.* 74(2), 483-494.
1045

1046 Henstock, T. J., Woods, A. W., White, R. S., 1993. The accretion of oceanic crust by episodic sill
1047 intrusion. *J. Geophys. Res.* 98, 4,143-4,161.
1048

1049 Herron, T. J., Stoffa, P. L., Buhl, P., 1980. Magma chamber and mantle reflections—East Pacific
1050 Rise. *Geophys. Res. Lett.* 7(11), 989-992.
1051

1052 Hess, H.H., 1962. The history of Ocean basins, in *Petrologic Studies*, Eds Engel, A.J.E., James,
1053 H.L., and Leonard, B.F., *Geol. Soc. Am.*, 599-620.
1054

1055 Holmes, R. C., Tolstoy, M., Cochran, J. R., Floyd, J. S., 2008. Crustal thickness variations along the
1056 Southeast Indian Ridge (100°–116° E) from 2D body wave tomography. *Geochem. Geophys.*
1057 *Geosyst.* 9, Q12020.
1058

1059 Jarchow, C. M., Thompson, G. A., 1989. The nature of the Mohorovicic discontinuity. *Annu. Rev.*
1060 *Earth Planet. Sci.* 17(1), 475-506.
1061

1062 Jian, H., Chen, Y. J., Singh, S. C., Li, J., Zhao, M., Ruan, A., Qiu, X., 2017. Seismic structure and
1063 magmatic construction of crust at the ultraslow spreading Southwest Indian Ridge at 50° 28'E. *J.*
1064 *Geophys. Res.* 122(1), 18-42.
1065

1066 Jousselin, D., Nicolas, A., 2000. The Moho transition zone in the Oman ophiolite-relation with
1067 wehrlites in the crust and dunites in the mantle. *Mar. Geophys. Res.* 21(3-4), 229-241.
1068

1069 Jousselin, D., Morales, L. F., Nicolle, M., Stephant, A., 2012. Gabbro layering induced by simple
1070 shear in the Oman ophiolite Moho transition zone. *Earth Planet. Sci. Lett.* 331, 55-66.
1071

1072 Karson, J. A., Collins, J. A., Casey, J. F., 1984. Geologic and seismic velocity structure of the
1073 crust/mantle transition in the Bay of Islands ophiolite complex. *J. Geophys. Res.* 89(B7), 6126-
1074 6138.
1075

1076 Kelemen, P. B., Koga, K., Shimizu, N. (1997). Geochemistry of gabbro sills in the crust-mantle
1077 transition zone of the Oman ophiolite: Implications for the origin of the oceanic lower crust. *Earth*
1078 *Planet. Sci. Lett.* 146(3-4), 475-488.
1079

1080 Kelemen, P.B., Matter, J.M., Teagle, D.A.H., Coggon, J.A., the Oman Drilling Project Science
1081 Team, 2020. *Proceedings of the Oman Drilling Project: College Station, TX (International Ocean*
1082 *Discovery Program).*
1083

1084 Kent, G. M., Harding, A. J., Orcutt, J. A., Detrick, R. S., Mutter, J. C., Buhl, P., 1994. Uniform
1085 accretion of oceanic crust south of the Garrett transform at 14° 15' S on the East Pacific Rise. *J.*
1086 *Geophys. Res.* 99(B5), 9097-9116.
1087

1088 Kent, G. M., Harding, A.J., Orcutt, J. A., 1990. Evidence for a smaller magma chamber beneath the
1089 East Pacific Rise at 9 30 N. *Nature* 344, 650-653.
1090

1091 Kempner, W. C., Gettrust, J. F., 1982. Ophiolites, synthetic seismograms, and ocean crustal
1092 structure: 1. Comparison of ocean bottom seismometer data and synthetic seismograms for the Bay
1093 of Islands ophiolite. *J. Geophys. Res.* 87(B10), 8447-8462.
1094

1095 Korenaga, J., Holbrook, W. S., Kent, G. M., Kelemen, P. B., Detrick, R. S., Larsen, H.-C., et al.,
1096 2000. Crustal structure of the southeast Greenland margin from joint refraction and reflection
1097 seismic tomography. *J. Geophys. Res.* 105(B9), 21591–21614.
1098

1099 Levander, A. R., 1988. Fourth-order finite-difference P-SV seismograms. *Geophysics* 53(11), 1425-
1100 1436.
1101

1102 Marjanović, M. et al., 2014. A multi-sill magma plumbing system beneath the axis of the East
1103 Pacific Rise, *Nat. Geosci.* 7, 825-829.
1104

1105 McBride, J. H., White, R. S., Henstock, T. J., Hobbs, R. W., 1994. Complex structure along a
1106 Mesozoic seafloor spreading ridge: BIRPS deep seismic reflection, Cape Verde abyssal plain.
1107 *Geophys. J. Int.* 119(2), 453-478.
1108

1109 Mehouchi, F., Singh, S.C., 2018. Water-rich sub-lithospheric melt channel in the equatorial
1110 Atlantic Ocean. *Nat. Geosci.* 11, 65–6.
1111

1112 Mithal, R., Mutter, J. C. (1989). A low-velocity zone within the layer 3 region of 118 Myr old
1113 oceanic crust in the western North Atlantic. *Geophys. J. Int.* 97(2), 275-294.
1114

1115 Mjelde, R., 1992. Shear waves from three-component ocean bottom seismographs off Lofoten,
1116 Norway, indicative of anisotropy in the lower crust. *Geophys. J. Int.* 110(2), 283-296.
1117

1118 Mohorovičić, A. 1910. Potres od 8. X 1909. Godišnje izvješće Zagrebačkog meteorološkog
1119 opservatorija za godinu 1909. 9/4, 1–56.
1120

1121 Morris, E., Detrick, R. S., Minshull, T. A., Mutter, J. C., White, R. S., Su, W., Buhl, P., 1993.
1122 Seismic structure of oceanic crust in the western North Atlantic. *J. Geophys. Res.* 98(B8), 13879-
1123 13903.
1124

1125 Mutter, J. C., Carton, H. D., 2013. The Mohorovicic discontinuity in ocean basins: Some
1126 observations from seismic data. *Tectonophysics* 609, 314-330.
1127

1128 Nedimović, M. R., Carbotte, S. M., Harding, A. J., Detrick, R. S., Canales, J. P., Kent, G. M.,
1129 Tischer, M., Diebold, J. B., Babcock, J. M., 2005. Frozen subcrustal magma lenses. *Nature* 436,
1130 1149-1152.
1131

1132 Neves, F., Singh, S.C., 1996. Sensitivity study of seismic reflection/refraction data, *Geophys. J. Int.*,
1133 126, 470-476.
1134

1135 Nicolas, A., Boudier, F., Ildefonse, B., 1996. Variable Moho depth in the Oman ophiolite:
1136 Implication for oceanic ridges. *J. Geophys. Res.* 101 (BB), 17941-17950.
1137

1138 Ohira, A., Kodaira, S., Nakamura, Y., Fujie, G., Arai, R., Miura, S., 2017. Structural variation of
1139 the oceanic Moho in the Pacific plate revealed by active-source seismic data. *Earth Planet. Sci. Lett.*
1140 476, 111-121.
1141

1142 Okazaki, K., Abe, N., Hatakeyama, K., Akamatsu, Y., Takazawa, E., Teagle, D. A., Kelemen, P.B.
1143 Coggon, J. A., 2018. Physical property of the fossilized crust-mantle transition zone from ICDP
1144 Oman Drilling Project Hole CM1A and CM2B. *AGUFM, 2018*, V11B-03.
1145

1146 Peng, C., Toksöz, M. N., 1995. An optimal absorbing boundary condition for elastic wave
1147 modeling. *Geophysics* 60(1), 296-301.
1148

1149 Penrose Conference participants, 1972. GSA Penrose Field Conference on Ophiolites. *Geotimes*,17,
1150 24–25.
1151

1152 Planert, L., Flueh, E. R., Reston, T. J., 2009. Along- and across-axis variations in crustal thickness
1153 and structure at the Mid-Atlantic Ridge at 5 °S obtained from wide-angle seismic tomography:
1154 Implications for ridge segmentation. *J. Geophys. Res.* 114, B09102.
1155

1156 Prodehl, C., Kennett, B., Artemieva, I. M., Thybo, H., 2013. 100 years of seismic research on the
1157 Moho. *Tectonophysics* 609, 9-44.
1158

1159 Quick, J. E., Denlinger, R. P., 1993. Ductile deformation and the origin of layered gabbro in
1160 ophiolites, *J. Geophys. Res.* 98, 14015-14027.
1161

1162 Raitt, R. W., 1956. Seismic-refraction studies of the Pacific Ocean Basin: Part I: Crustal thickness
1163 of the Central Equatorial Pacific. *Geol. Soc. Am. Bull.* 67(12), 1623-1640.
1164

1165 Schanker, G., Lippsett, L., 2016. The Quest for the Moho. *Oceanus* 52(1), 44.
1166

1167 Sereno, T. J., Orcutt, J. A., 1985. Synthetic seismogram modelling of the oceanic Pn phase. *Nature*
1168 316(6025), 246-248.
1169

1170 Shipp, R. M., Singh, S. C., 2002. Two-dimensional full wavefield inversion of wide-aperture
1171 marine seismic streamer data. *Geophys. J. Int.* 151(2), 325-344.
1172

1173 Singh, S. C., Collier, J. S., Harding, A. J., Kent, G. M., Orcutt, J. A., 1999. Seismic evidence for a
1174 hydrothermal layer above the solid roof of the axial magma chamber at the southern East Pacific
1175 Rise. *Geology* 27(3), 219-222.
1176

1177 Singh, S.C., Harding, A., Kent, G., Sinha, M.C., Combier, V., Hobbs, R., Barton, P., White, R.,
1178 Tong, V., Pye, J., Orcutt, J., 2006. Seismic reflection images of Moho underlying melt sills at the
1179 East Pacific Rise, *Nature* 442, 287-290.
1180

1181 Spudich, P., Orcutt, J., 1980. A new look at the seismic velocity structure of the oceanic crust. *Rev.*
1182 *Geophys.* 18(3), 627-645.
1183

1184 Stoffa, P., Buhl, P., 1979. Two-ship multi-channel seismic experiments for deep crustal studies:
1185 expanding spread and constant offset profiles, *J. Geophys. Res.* 84, 7645-7660.
1186

1187 Stoffa, P., Buhl, P., Diebold, J. B., Wenzel, F., 1981. Direct mapping of seismic data to the domain
1188 of intercept time and ray parameter: A plane wave decomposition, *Geophysics* 46, 255-267.
1189

1190 Taylor, M., Singh, S.C., 2002. Composition and microstructure of magma bodies from effective
1191 medium theory. *Geophys. J. Int.* 149, 15-21.
1192

1193 Thomson, C., Clarke, T., Garmany, J., 1986. Observations on seismic wave equation and reflection
1194 coefficient symmetries in stratified media. *Geophys. J. Int.* 86(2), 675-686.
1195

1196 Toomey, D. R., Purdy, G. M., Solomon, S. C., Wilcock, W. S., 1990. The three-dimensional
1197 seismic velocity structure of the East Pacific Rise near latitude 9° 30' N. *Nature* 347(6294), 639-645.
1198

1199 Vaddineni, V., Singh, S. C., Grevemeyer, I., Audhkhasi, P., Papenberg, C., 2020. Evolution of the
1200 crustal structure from 0-27 Ma in the equatorial Atlantic Ocean at 2° 43' S. *J. Geophys. Res.*,
1201 DOI:10.1029/2020JB0211390 .
1202

1203 Van Avendonk, H. J. A., Harding, A. J., Orcutt, J. A., McClain, J. S., 2001. Contrast in crustal
1204 structure across the Clipperton transform fault from travel time tomography. *J. Geophys. Res.*
1205 106(B6), 10,961–10,981.
1206

1207 Vera, E.E., Vera, Mutter, J., Buhl, J., Orcutt, J., Harding, A., Kappus, M.E., Detrick, R.S., Brocher,
1208 T. M., 1990. The structure of 0 to 0.2 m.y. old oceanic crust at 9° N on the East Pacific Rise from
1209 expanded spread profiles, *J. Geophys. Res.* 95, 15,529-15,556.

1210

1211 White, R. S., McKenzie, D., O'Nions, R. K., 1992. Oceanic crustal thickness from seismic
1212 measurements and rare earth element inversions. *J. Geophys. Res.* 97(B13), 19683-19715.